EXTENSION OF THE ENTROPY VISCOSITY METHOD TO THE MULTI-D

EULER EQUATIONS AND THE SEVEN EQUATIONS MODEL.

A Dissertation

by

MARC-OLIVIER GERARD DELCHINI

Submitted to the Office of Graduate and Professional Studies of
Texas A&M University
in partial fulfillment of the requirements for the degree of

DOCTOR OF PHILOSOPHY

Co-Chairs of Committee,	Jean C. Ragusa
	Jean Luc Guermond
Committee Members,	Jim Morel
	Yassin Hassan
	Ray Berry
Head of Department,	Yassin Hassan

December 2014

Major Subject: Nuclear Engineering Department

ABSTRACT

Lorem ipsum dolor sit amet, consectetur adipiscing elit. Integer lectus quam, condimentum quis bibendum eu, sollicitudin eget lacus. Praesent non sodales odio. Class aptent taciti sociosqu ad litora torquent per conubia nostra, per inceptos himenaeos. Nulla ac luctus sapien. Morbi cursus sapien eget lorem fermentum hendrerit. Nam ac erat dui, in cursus velit. Vivamus hendrerit porttitor nisi, ut porttitor lorem volutpat eget. In ligula ligula, euismod ut condimentum sit amet, pulvinar sit amet diam. Pellentesque interdum, ipsum ullamcorper consequat dignissim, sem arcu egestas mauris, vitae interdum sem tortor ut ante. Nunc blandit laoreet nisi, non rutrum lorem hendrerit quis. Cras nunc diam, convallis et feugiat at, auctor id libero. Nunc facilisis massa eu eros imperdiet vestibulum. Vestibulum ante ipsum primis in faucibus orci luctus et ultrices posuere cubilia Curae; Donec non velit vitae tortor blandit semper.

Etiam vitae dolor nulla. Ut eros odio, rhoncus eget placerat vitae, elementum ac ante. Proin vitae odio eu nisl pharetra mattis. Pellentesque habitant morbi tristique senectus et netus et malesuada fames ac turpis egestas. Phasellus fermentum lacus consectetur neque consequat ullamcorper. Cras blandit urna non dui consequat molestie. Curabitur viverra nibh at nisi semper faucibus. Nam egestas mauris a enim dignissim nec consectetur tortor rutrum. Mauris at nisi in est luctus congue ut mattis est. Ut pretium, mi quis elementum cursus, ante eros suscipit ligula, ut porttitor elit leo sed turpis. Nam sed dui ligula.

DEDICATION

This is an optional page. Lorem ipsum dolor sit amet, consectetur adipiscing elit. Integer lectus quam, condimentum quis bibendum eu, sollicitudin eget lacus. Praesent non sodales odio. Class aptent taciti sociosqu ad litora torquent per conubia nostra, per inceptos himenaeos. Nulla ac luctus sapien. Morbi cursus sapien eget lorem fermentum hendrerit. Nam ac erat dui, in cursus velit. Vivamus hendrerit porttitor nisi, ut porttitor lorem volutpat eget. In ligula ligula, euismod ut condimentum sit amet, pulvinar sit amet diam. Pellentesque interdum, ipsum ullamcorper consequat dignissim, sem arcu egestas mauris, vitae interdum sem tortor ut ante. Nunc blandit laoreet nisi, non rutrum lorem hendrerit quis. Cras nunc diam, convallis et feugiat at, auctor id libero. Nunc facilisis massa eu eros imperdiet vestibulum. Vestibulum ante ipsum primis in faucibus orci luctus et ultrices posuere cubilia Curae; Donec non velit vitae tortor blandit semper.

Etiam vitae dolor nulla. Ut eros odio, rhoncus eget placerat vitae, elementum ac ante. Proin vitae odio eu nisl pharetra mattis. Pellentesque habitant morbi tristique senectus et netus et malesuada fames ac turpis egestas. Phasellus fermentum lacus consectetur neque consequat ullamcorper. Cras blandit urna non dui consequat molestie. Curabitur viverra nibh at nisi semper faucibus. Nam egestas mauris a enim dignissim nec consectetur tortor rutrum. Mauris at nisi in est luctus congue ut mattis est. Ut pretium, mi quis elementum cursus, ante eros suscipit ligula, ut porttitor elit leo sed turpis. Nam sed dui ligula.

ACKNOWLEDGEMENTS

NOMENCLATURE

B/CS   Bryan/College Station

HSUS   Humane Society of the United States

P   Pressure

T   Time

TVA   Tennessee Valley Authority

TxDOT   Texas Department of Transportation

This page is optional.

TABLE OF CONTENTS

LIST OF FIGURES

LIST OF TABLES

1. INTRODUCTION: THE IMPORTANCE OF RESEARCH

1.1   This is a Very Long Section Title This is a Very Long Section Title This is a Very Long Section Title

Hyperbolic systems of equations are encountered in various engineering fields (extraction of oil, turbine technology, nuclear reactors, etc . . .). Improving numerical solution techniques for such equations are an ongoing topic of research. This is obviously the case for fluid equations. Being able to accurately solve and predict the behavior of a fluid in a turbine or in a reactor, for example, can lead to a safe decrease in conservative safety margins, which translates into a decrease in production cost. Thus, we can see the importance of having a good understanding of the mathematical theory behind these wave-dominated systems of equations, and also, the importance of developing robust and accurate numerical methods.

A large number of theoretical studies has shown the role played by characteristic equations and the corresponding eigenvalues on how and at what speed the physical information propagates: physical shocks or discontinuities can form, leading to unphysical instabilities and oscillations that pollute the numerical solution due to entropy production [19]. Thus, a question rises: how to accurately resolve shocks and conserve the physical solution at the same time? A lot of work is available in the literature and include Riemann solvers, Godunov-type fluxes, flux limiter and artificial viscosity methods. Toro's book [19] gives a good overview of the theory related to hyperbolic systems of equations and focuses on Riemann solvers and Godunov-type fluxes that can be used with discontinuous spatial discretizations: finite volume (FV) and discontinuous Galerkin finite element method (DGFEM). Flux limiters [**?**, **?**] can achieve high-order accuracy with DGFEM [**?**] but suffer from some drawbacks: diffi-

culties were found to reach steady-state solution when using time-stepping schemes and generalization to unstructured grids is not obvious [**?**]. The artificial viscosity method was first introduced by Neumann and Richtmeyer [**?**] but was found over-dissipative and, thus, abandoned. It is only, later with the development of high-order schemes and because of their simple implementation that they have regained interest: Lapidus [**?**, **?**] developed a high-order viscosity method by making the viscosity coefficient proportional to the gradient of the velocity in 1-D. Lohner et al. [**?**] extended this concept to multi-dimension by introducing a vector that will measure the direction of maximum change in the absolute value of the velocity norm, so that shear layers are not smeared. Pressure-based viscosities were also studied [**?**] where the viscosity coefficient is set proportional to the Laplace of pressure, allowing to detect curvature changes in the pressure profile. Since pressure is nearly constant but in shocks, it is a good indicator of the presence of a shock. Recently, Reisner et al. [**?**] introduced the C-method for the compressible Euler equations with artificial dissipative terms: instead of computing the viscosity coefficient on the fly as for Lapidus and pressure-based methods, a partial differential equation (PDE) is added to the original system of equations. This additional PDE allows to solve for the viscosity coefficient and contains a source term that is function of the gradient of velocity. The method seems to yield good results in 1-D for a wide range of tests. Guermond et .al [8, 9, **?**] proposed an entropy-based viscosity method for conservative hyperbolic system of equations: artificial dissipative terms are added to the system of equations with a viscosity coefficient modulated by the entropy production that is known to be large in shocks and small everywhere else. The method was successfully applied in various schemes [9, **?**, 20] and showed high-order convergence with smooth solutions. Results using the ideal gas equation of state were run for 1-D Sod tube and showed good agreement with the exact solutions. 2-D tests were also performed on

unstructured grids and behaved very satisfactorily [20]. The method is fairly simple to implement and is consistent with the entropy inequality.

The objective of this research is to solve hyperbolic system of equations using a continuous Galerkin finite element method (CGFEM) and an implicit temporal discretization under the Moose framework [3]. We are particularly interested in simulating the flow behavior occurring in nuclear reactors. The set of equations that will be considered are the multi-D Euler equations with variable area [19] and the multi-D seven equations model for two-phase fluids [16]. These systems of equations are well defined in a sense that they possess real eigenvalues. To numerically solve these equations, we need to rely on a numerical method that will allow us to resolve shocks and discontinuity that may form. More importantly, we need a method that is accurate for a wide range of Mach numbers and is not restricted to any type of equation of state. These previous requirements can be hard to fulfill. Numerical methods are often tested with the ideal gas equation of state which can not be used for liquid phase. The difficulty rises once a numerical method used for resolving shocks, is required to work for low Mach flows that are isentropic: in this particular case, a compressible model is used to simulate a flow in the incompressible limit. Recent publications [?, ?] highlighted the difficulties related to such a choice: asymptotic studies have shown that some of the numerical methods become ill-scaled in the low Mach limit, making the numerical solution unphysical. For example, the Roe scheme requires a fix in the low Mach limit while conserving its accuracy when shocks occur [?].

We propose to use the entropy-based viscosity method introduced by Guermond et al. to solve for the hyperbolic systems previously enumerated since the method has shown good results when used for solving the multi-D Euler equations with various discretization schemes. More importantly, it is simple to implement, can be used

with unstructured grids, and its dissipative terms are consistent with the entropy minimum principle and proven valid for any equation of state under certain conditions [5]. However, a few questions remains: the low Mach limit has not been investigated and the current definition requires an analytical expression of the entropy which can be difficult to obtain for some equation of state. These two issues will be addressed. A particular attention will be brought to the low Mach problem and the available literature related to the asymptotic limit of the Navier-Stokes [?] and Euler equations [?, ?] should be of great insight in order to understand how the dissipative terms behave.

It is also proposed to investigate how the entropy viscosity method can be applied to the multi-D radiation-hydrodynamic equations [14]. These equations are known to develop solutions with shocks [2]. They consist of coupling the multi-D Euler equations with a radiation-diffusion equation through some source terms. Most of the current solvers are based on the study of the hyperbolic terms in order to derive a Riemann-type solver [17]. Flux-limiter technique [10] are also used and suffer from the same drawbacks as for the pure multi-D Euler equations. Therefore, it will be valuable to assess how the entropy viscosity method can adapt to this multi-physics system, and if successful, will offer an alternative to the current available numerical methods.

Thus, the proposal is organized as follows: Section 1 will recall the main feature of the current version of the entropy-based viscosity method. Section 2 will introduce the system of equations under considerations. A short description of the equations and their properties will be given. In Section 3, the problem formulation is discussed for each system of equations and suggestions of test cases are given in order to test the numerical method.

2. LITERATURE REVIEW: THE IMPORTANCE OF RESEARCH PART TWO- THIS IS DESIGNED TO TEST LONG TITLES IN THE TOC

Text goes here.

2.1 Introduction

Over the past years an increasing interest raised for computational methods that can solve both compressible and incompressible flows. In engineering applications, there is often the need to solve for complex flows where a near incompressible regime or low Mach flow coexists with a supersonic flow domain. For example, such flow are encountered in aerodynamic in the study of airships. In the nuclear industry, flows are nearly the incompressible regime but compressible effects cannot be neglected because of the heat source and thus needs to be accurately resolved.

When solving the multi-D Euler equations for a wide range of Mach numbers, multiple problems have to address: stability, accuracy and acceleration of the convergence in the low Mach regime. Because of the hyperbolic nature of the equations, shocks can form during transonic and supersonic flows, and require the use of the numerical methods in order to stabilize the scheme and correctly resolve the discontinuities. The literature offers a wide range of stabilization methods: flux-limiter [**?**, **?**], pressure-based viscosity method ([**?**]), Lapidus method ([**?**, **?**, **?**]), and the entropy-viscosity method([8, 9]) among others. These numerical methods are usually developed using simple equation of states and tested for transonic and supersonic flows where the disparity between the acoustic waves and the fluid speed is not large since the Mach number is of order one. This approach leads to a well-known accuracy problem in the low Mach regime where the fluid velocity is smaller that the speed of sound by multiple order of magnitude. The numerical dissipative terms become ill-scaled

in the low Mach regime and lead to the wrong numerical solution by changing the nature of the equations solved. This behavior is well documented in the literature [?, ?, ?] and often treated by performing a low Mach asymptotic study of the multi-D Euler equation. This method was originally used [?] to show convergence of the compressible multi-D Euler equations to the incompressible ones. Thus, by using the same method, the effect of the dissipative terms in the low Mach regime, can be understood and, when needed, a fix is developed in order to ensure the convergence of the equations to the correct physical solution. This approach was used as a fixing method for multiple well known stabilization methods alike Roe scheme ([?]) and SUPG [?] while preserving the original stabilization properties of shocks.

We propose, through this paper, to investigate how the entropy viscosity method, when applied to the multi-D Euler equations with variable area, behaves in the low Mach regime. This method was initially introduced by Guermond et al. to solve for the hyperbolic systems and has shown good results when used for solving the multi-D Euler equations with various discretization schemes. More importantly, it is simple to implement, can be used with unstructured grids, and its dissipative terms are consistent with the entropy minimum principle and proven valid for any equation of state under certain conditions [5].

This paper is organized as follows: in Section 2.2 the current definition of the entropy viscosity method is recalled, and inconsistency with the low Mach regime are pointed out. Since our interest is in the variable area version of the multi-D Euler equation, the reader is guided trough the steps leading to the derivation of the dissipative terms on the model of [5]. Then in Section 2.3, a new definition of the viscosity coefficient is introduced and derived from a low Mach asymptotic study. After detailing the spatial and temporal discretization method in Section 2.4, 1- and 2-D numerical results are presented in Section 2.5 for a wide range of Mach numbers: low Mach flow

over a cylinder and a circular bump, and supersonic flow in a compression corner [**?**].
Convergence studies are performed in 1-D, in order to demonstrate the accuracy of
the solution.

For purpose of clarity, the multi-D Euler equations with variable area are recalled in
Eq. (2.1) and the corresponding variables are defined:

$$
\begin{cases}
\partial_t\left(\rho A\right) + \vec{\nabla}\cdot\left(\rho\vec{u}A\right) = 0 \\
\partial_t\left(\rho\vec{u}A\right) + \vec{\nabla}\cdot\left[\left(\rho\vec{u}\otimes\vec{u} + P\mathbf{I}\right)A\right] = P\vec{\nabla}A \\
\partial_t\left(\rho E A\right) + \vec{\nabla}\cdot\left[\vec{u}\left(\rho E + P\right)A\right] = 0 \\
P = P\left(\rho, e\right)
\end{cases}
\tag{2.1}
$$

where ρ, $\rho\vec{u}$ and ρE are the density, the momentum and the total energy, respectively,
and will be referred to as the conservative variables. The pressure P is computed
with an equation of state expressed in function of the density ρ and the specific
internal energy e. The tensor product $\vec{a}\otimes\vec{b}$ is taken with the following convention:
$(\vec{a}\otimes\vec{b})_{i,j} = a_i b_j$. Lastly, the terms ∂_t, $\vec{\nabla}$, $\vec{\nabla}\cdot$ and $\mathbf{I}$ denote the temporal derivative, the
gradient and divergent operators, and the identity tensor, respectively. The variable
area A is assumed spatial dependent.

2.2   The Entropy Viscosity Method

2.2.1   Background

In this section, the entropy-based viscosity method [8, 9, **?**] is recalled for the
multi-D Euler equations (with constant area A) [20]. The entropy-based viscosity
method consists of adding dissipative terms, with a viscosity coefficient modulated
by the entropy production which allows high-order accuracy when the solution is
smooth. Thus, two questions arise: (i) how are the viscosity dissipative terms derived
and (ii) how to numerically compute the entropy production. Answers to the first

7

question can be found in [5] by Guermond et al., that details the proof leading to the derivation of the artificial dissipative terms (Eq. (2.2)) consistent with the entropy minimum principle theorem. The viscous regularization obtained is valid for any equation of state as long as the opposite of the physical entropy function, s, is convex with respect to the internal energy e and the specific volume $1/\rho$. As for the entropy production, it is locally evaluated by computing the local entropy residual $D_e(\vec{x}, t)$ defined in Eq. (2.4), that is known to be peaked in shocks [19].

$$
\begin{cases}
\partial_t (\rho) + \vec{\nabla} \cdot (\rho \vec{u}) = \vec{\nabla} \cdot \left(\kappa \vec{\nabla} \rho \right) \\
\partial_t (\rho \vec{u}) + \vec{\nabla} \cdot (\rho \vec{u} \otimes \vec{u} + P\mathbf{I}) = \vec{\nabla} \cdot \left(\mu \rho \vec{\nabla}^s \vec{u} + \kappa \vec{u} \otimes \vec{\nabla} \rho \right) \\
\partial_t (\rho E) + \vec{\nabla} \cdot [\vec{u} (\rho E + P)] = \vec{\nabla} \cdot \left(\kappa \vec{\nabla} (\rho e) + \frac{1}{2} ||\vec{u}||^2 \kappa \vec{\nabla} \rho + \rho \mu \vec{u} \vec{\nabla} \vec{u} \right) \\
P = P(\rho, e)
\end{cases}
\tag{2.2}
$$

where κ and μ are local positive viscosity coefficients. $\vec{\nabla}^s \vec{u}$ denotes the symmetric gradient operator that guarantees the method to be rotational invariant [5].

In the current version of the method, κ and μ are set equal, so that the above viscous regularization (Eq. (2.2)) is equivalent to the parabolic regularization [1] when considering the 1-D form of the equation. The current definition includes a first-order viscosity coefficient referred to with the subscript max, and a high-order viscosity coefficient referred to with the subscript e. The first-order viscosity coefficients μ_{max} and κ_{max} are proportional to the local largest eigenvalue $||\vec{u}|| + c$ and equivalent to an upwind-scheme (see Eq. (2.3)), when used, which is known to be over-dissipative and monotone [19]:

$$
\mu_{max}(\vec{r}, t) = \kappa_{max}(\vec{r}, t) = \frac{h}{2} (||\vec{u}|| + c),
\tag{2.3}
$$

where h is defined as the ratio of the grid size to the polynomial order of the test functions used.

The second-order viscosity coefficients κ_e and μ_e are set proportional to the entropy production that is evaluated by computing the local entropy residual D_e. It also includes the interfacial jump of the entropy flux J that will allow to detect any discontinuities other than shocks:

$$\mu_e(\vec{r},t) = \kappa_e(\vec{r},t) = h^2 \frac{\max\left(|D_e(\vec{r},t)|, J\right)}{||s - \bar{s}||_\infty} \text{ with } D_e(\vec{r},t) = \partial_t s + \vec{u} \cdot \vec{\nabla} s \qquad (2.4)$$

where $||\cdot||_\infty$ and $\bar{\cdot}$ denote the infinite norm operator and the average operator over the entire computational domain, respectively. The definition of the jump J is discretization-dependent and examples of definition can be found in [20] for DGFEM. The denominator $||s - \bar{s}||_\infty$ is used for dimensionality purposes and should not be of the same order as h, on penalty of loosing the high-order accuracy. Currently, there are no theoretical justification for choosing the denominator.

The definition of the viscosity coefficients μ and κ is function of the first- and second-order viscosity coefficients as follows:

$$\mu(\vec{r},t) = \min\left(\mu_e(\vec{r},t), \mu_{max}(\vec{r},t)\right) \text{ and } \kappa(\vec{r},t) = \min\left(\kappa_e(\vec{r},t), \kappa_{max}(\vec{r},t)\right). \qquad (2.5)$$

This definition allows the following properties. In shock regions, the second-order viscosity coefficient experiences a peak because of entropy production, and thus, saturates to the first-order viscosity that is known to be over-dissipative and will smooth out oscillations. Anywhere else, the entropy production being small, the viscosity coefficients μ and κ are of order h^2.

Using the above definition of the entropy-based viscosity method, high-order accu-

racy was demonstrated and excellent results were obtained with 1-D Sod shock tubes and various 2-D tests [8, 9, 20].

2.2.2   Issues in the Low-Mach Regime

In the Low-Mach Regime, the flow is known to be isentropic resulting in very little entropy production. Since the entropy viscosity method is directly based on the evaluation of the local entropy production, it will be interested to study how the entropy viscosity coefficients μ and κ scale in the low Mach regime. Mathematically, it means that the entropy residual D_e will be very small, so will be the denominator $||s - \bar{s}||_\infty$, thus making the ratio, used in the definition of the viscosity coefficients Eq. (2.4), undetermined. Therefore, the current definition of the viscosity coefficients seems unadapted to subsonic flow and could lead to ill-scaled dissipative terms. A solution would be to recast the entropy residual as a function of other variables in order to have more freedom in the choice of the normalization parameter. With this approach, the viscosity coefficients are still defined proportional to the entropy residual that is a good indicator of the flow type (subsonic, transonic and supersonic flow). Plus, a different normalization parameter could be chosen, based on a low Mach asymptotic study so that the viscosity coefficients are well-scaled in the low Mach asymptotic limit (see Section 2.3).

2.2.3   The dissipative-terms for the multi-D Euler equations with variable area

One of the focus of this paper is to investigate the application of the entropy viscosity method to the multi-D Euler equations with variable area. The variable area version of the Euler equations is mostly used in 1-D and 2-D for obvious reasons, and differs from Eq. (2.1) by the momentum equation as shown in Eq. (2.6), that contains a non-conservative term proportional to the area gradient. For the purpose of this paper, the variable area is assumed to be a smooth function and only spatial

dependent. An example can be found in [16] where a fluid flows through a 1-D convergent-divergent nozzle and reaches a steady-state solution.

$$
\begin{cases}
\partial_t \left(\rho A \right) + \vec{\nabla} \cdot (\rho \vec{u} A) = 0 \\
\partial_t \left(\rho \vec{u} A \right) + \vec{\nabla} \cdot [A \left(\rho \vec{u} \otimes \vec{u} + P\mathbf{I} \right)] = P\vec{\nabla} A \\
\partial_t \left(\rho E \right) + \vec{\nabla} \cdot [\vec{u} \left(\rho E + P \right)] = 0
\end{cases}
\tag{2.6}
$$

The application of the entropy viscosity method to the above system of equations is expected to be straightforward since it degenerates to the Eq. (2.1) when assuming a constant area. Details of the derivations of the dissipative terms are available to the reader in Appendix **??** and are very similar to what was done in [5]. An entropy residual is derived without the dissipative terms. Then, the same entropy residual is re-derived after adding dissipative terms to each equation of the system given in Eq. (2.6), and the entropy minimum principle is used as a condition to obtain a definition for each of the dissipative terms. The final result including the dissipative terms is given in Eq. (2.7):

$$
\begin{cases}
\partial_t \left(\rho A \right) + \vec{\nabla} \cdot (\rho \vec{u} A) = \vec{\nabla} \cdot \left(A \kappa \vec{\nabla} \rho \right) \\
\partial_t \left(\rho \vec{u} A \right) + \vec{\nabla} \cdot [A \left(\rho \vec{u} \otimes \vec{u} + P\mathbf{I} \right)] = P\vec{\nabla} A + \vec{\nabla} \cdot \left[A \left(\mu \rho \vec{\nabla}^s \vec{u} + \kappa \vec{u} \otimes \vec{\nabla} \rho \right) \right] \\
\partial_t \left(\rho E \right) + \vec{\nabla} \cdot [\vec{u} \left(\rho E + P \right)] = \vec{\nabla} \cdot \left[A \left(\kappa \vec{\nabla} \left(\rho e \right) + \frac{1}{2} ||\vec{u}||^2 \kappa \vec{\nabla} \rho + \rho \mu \vec{u} \vec{\nabla} \vec{u} \right) \right]
\end{cases}
\tag{2.7}
$$

The dissipative terms are very similar to the ones obtained for the multi-D Euler equations: each dissipative flux is multiplied by the variable area A in order to ensure conservation of the flux. When assuming a constant area, Eq. (2.2) is retrieved. The definition of the viscosity coefficients μ and κ is explained in Section 2.3.2.

2.3 All-speed Reformulation of the Entropy Viscosity Method

In this section, the entropy residual D_e is recast as a function of the pressure, the density and the speed of sound. Then, a low Mach asymptotic study of the multi-D Euler equations is performed in order to derive the correct normalization parameter.

2.3.1 New Entropy Production Residual

The first step in defining a viscosity coefficient that behaves well in the low mach limit is to recast the entropy residual in terms of the thermodynamic variables as shown in Eq. (2.8):

$$D_e(\vec{r},t) = \partial_t s + \vec{u} \cdot \vec{\nabla} s = \frac{s_e}{P_e} \left(\underbrace{\frac{dP}{dt} - c^2 \frac{d\rho}{dt}}_{\tilde{D}_e(\vec{r},t)} \right), \tag{2.8}$$

where $\frac{d\cdot}{dt}$ denotes the material or total derivative, and P_e is the partial derivative of pressure with respect to internal energy. The steps that lead to the new formulation of the entropy residual D_e can be found in Appendix **??**.

The entropy residual D_e and $\tilde{D}_e$ are proportional to each other and therefore will experience the same variation when taking the absolute value. Thus, locally evaluating $\tilde{D}_e$ instead of D_e should allow us to measure the entropy production point wise. This new expression given in Eq. (2.8) has multiple advantages:

- an analytical expression of the entropy function is not longer needed: the entropy residual $\tilde{D}_e$ is evaluated using the local values of the pressure, the density and the speed of sound. Deriving an entropy function for some complex equation of states can be difficult.

- with the proposed expression of the entropy residual function of pressure and

density, additional normalizations suitable for low Mach flows of the entropy residual can be devised. Examples include the pressure itself, or combination of the density, the speed of sound and the norm of the velocity: ρc^2, $\rho c ||\vec{u}||$ and $\rho ||\vec{u}||^2$.

The viscosity coefficients μ and κ are now defined proportional to the new entropy residual $\tilde{D}_e$ on the model of Eq. (2.4) as follows:

$$\mu\left(\vec{(r)}, t\right) = \kappa\left(\vec{(r)}, t\right) = h^2 \frac{\max\left(\tilde{D}_e, J\right)}{n(P)} \tag{2.9}$$

where $n(P)$ is a normalization parameter to determine and all other variables were defined previously.

As mentioned earlier, the normalization parameter $n(P)$ must be of the same units as the pressure for the viscosity coefficients to have the unit of a dynamic viscosity (m^2/s). Multiples options are available to us: P, ρc^2, $\rho c ||\vec{u}||$ and $\rho ||\vec{u}||^2$. The choice of the normalization parameter cannot be random if the definition of the viscosity coefficient is wanted to be well-scaled for a wide range of Mach numbers. For example, by choosing $n(P) = \rho ||\vec{u}||^2$, the viscosity coefficient will become very large as the Mach number decreases which would be unnecessary since the equations will not develop any shock or discontinuity. Therefore, it is proposed to carry, in Section 2.3.2, a low-Mach asymptotic study of the multi-D Euler equations in order to determine the correct expression for the normalization parameter $n(P)$.

2.3.2 Low-Mach asymptotic study of the multi-D Euler equations

The asymptotic study requires the multi-D Euler equations to be non dimensionalized: the objective is to make the Mach number appears and thus, use a polynomial expansion of the variables as a function of the Mach number in order to derive the

leading, first- and second-order equations. Before detailing the steps of the asymp-
totic method, let us have a closer look at the system of equations under consideration.
The initial system of equations is composed of the multi-D Euler equations. For sta-
bility purpose, artificial dissipative terms are added to each equation as explained
in Section 2.2. The resulting system of equations is alike the multi-D Navier-Stokes
equations in a sense that it contains second-order derivative terms. Thus, it would
be interesting to look at the steps employed in the asymptotic study of the multi-
D Navier-Stokes equations in order to understand how the dissipative terms are
treated. Fortunately, this process is well-documented in the literature [?, ?, ?] for
both multi-D Euler equations and Navier-Stokes equations. The work presented here
is mainly inspired of [?] that focuses on the asymptotic study in the low Mach regime
of Navier-Stokes equations. During the derivation, the reader has to keep in mind
that the objective of this section is to derive a normalization parameter for the defi-
nition of the viscosity coefficients so that the multi-D Euler equations degenerate to
the incompressible system of equations, which implies that the dissipative terms are
well-scaled. The main steps of the derivation are presented in the following of this
section:

To express Eq. (2.2) in dimensionless variables, the following dimensional variables
are introduced:

$$
\begin{aligned}
\rho &= \frac{\rho^*}{\rho_\infty}, \, P = \frac{P^*}{\rho_\infty c_\infty^2}, \, \mu = \frac{\mu^*}{\mu_\infty}, \, , \, E = \frac{E^*}{c_\infty^2}, \, \mu = \frac{\mu^*}{\mu_\infty}, \\
\kappa &= \frac{\kappa^*}{\kappa_\infty}, \, x = \frac{x^*}{L_\infty}, \, t = \frac{t^*}{L_\infty/u_\infty}, \, u = \frac{u^*}{u_\infty}
\end{aligned}
\tag{2.10}
$$

where the subscript ∞ and the upper script $*$ denote the far field or stagnation
quantities and the dimensionless variables, respectively. The reference quantities are
chosen such that the non dimensional flow quantities are of order one for any low

reference-Mach number

$$M_\infty = \frac{u_\infty^*}{c*_\infty} \tag{2.11}$$

where c_∞^* is a reference value for the speed of sound.

Then, using the non dimensional quantities and the multi-D Euler equations from Eq. (2.2) , the following non dimensional form is obtained:

$$
\begin{cases}
\partial_t \rho + \nabla(\rho\vec{u}) = \frac{1}{Re_\infty Pr_\infty}\nabla \cdot (\kappa\nabla\rho) \\
\partial_t(\rho\vec{u}) + \nabla(\rho\vec{u}\otimes\vec{u}) + \frac{1}{M_\infty^2}\nabla(P) = \frac{1}{Re_\infty}\nabla(\rho\mu\nabla\vec{u}) + \frac{1}{Re_\infty Pr_\infty}\nabla \cdot (\vec{u}\otimes\kappa\nabla\rho) \\
\partial_t(\rho E) + \nabla \cdot [\vec{u}(\rho E + P)] = \frac{1}{Re_\infty Pr_\infty}\nabla \cdot (\kappa\nabla(\rho e)) + \frac{\tilde{M}_\infty^2}{Re_\infty}\nabla \cdot (\vec{u}\rho\mu\nabla\vec{u}) \\
+ \frac{M_\infty^2}{2Re_\infty Pr_\infty}\nabla \cdot (\kappa u^2\nabla\rho) \\
P = (\gamma - 1)(\rho E + M_\infty^2\rho u^2)
\end{cases}
$$

where the *numerical* Reynolds (Re_∞) and Prandtl (Pr_∞) numbers are defined as follows:

$$Re_\infty = \frac{u_\infty L_\infty}{\mu_\infty} \text{ and } Pr_\infty = \frac{\mu_\infty}{\kappa_\infty}. \tag{2.12}$$

Since it is chosen to have the same definition for both μ and κ the numerical Prandtl number is unconditionally equal to one: $Pr_\infty = 1$.

Once the dimensionless equations are obtained, the next step consists of expanding each variable in term of the Mach number (example given in Eq. (2.13) for the pressure P) in order to derive the leading, first- and second-order equations.

$$P(\vec{r}, t) = P_0(\vec{r}, t) + P_1(\vec{r}, t)M_\infty + P_2(\vec{r}, t)M_\infty^2 + \dots \text{ with } M_\infty \to 0 \tag{2.13}$$

Before deriving the leading-order equation, a choice needs to be made on how the numerical Reynolds number scales. Multiple options are available to us and a few

example are given: $Re_\infty = M_\infty$, or $Re_\infty = M_\infty^{-1}$ or $Re_\infty = 1$. Let us assume for academy purpose that the numerical Reynolds number scales as the inverse of the Mach number square: $Re_\infty = M_\infty^{-2}$. The best way to evaluate the impact of this choice on the equations, is to look at the momentum equation and try to derive the order M_∞^{-2}:

$$\vec{\nabla} P_0 = \vec{\nabla}\cdot(\rho_0\mu_0\vec{\nabla}\vec{u}_0 + \vec{u}_0 \otimes \vec{\nabla}\rho_0) \tag{2.14}$$

which is known to be ([?])

$$\vec{\nabla} P_0 = 0 \tag{2.15}$$

It is clear that Eq. (2.14) and Eq. (2.15) will not yield the same result. The same conclusion is drawn when deriving the order M_∞^{-1} of the momentum equation, making our initial assumption not suitable. From the above result, it is understood that the numerical Reynolds number has to scale as one so that it does not affect the orders M_∞^{-2} and M_∞^{-1} of the momentum equations: $Re_\infty = 1$. Thus, with such assumption, Eq. (2.12) implies:

At order M_∞^{-2}:
$$\vec{\nabla} P_0 = 0$$

At order M_∞^{-1}:
$$\vec{\nabla} P_1 = 0$$

At leading-order:

$$\partial_t\rho_0 + \vec{\nabla}\cdot(\rho_0\vec{u}_0) = \vec{\nabla}\cdot(\kappa_0\vec{\nabla}\rho_0)$$

$$\partial_t(\rho_0\vec{u}_0) + \vec{\nabla}\cdot(\rho_0\vec{u}_0 \otimes \vec{u}_0) + \vec{\nabla} P_2 = \vec{\nabla}\cdot(\rho_0\mu_0\vec{\nabla}\vec{u}_0 + \vec{u}_0 \otimes \vec{\nabla}\rho_0)$$

$$\partial_t(\rho_0 E_0) + \vec{\nabla}\cdot[\vec{u}_0(\rho_0 E_0 + P_0)] = \vec{\nabla}\cdot(\kappa_0\vec{\nabla}(\rho_0 e_0))$$

Under this form, the dissipative terms only affect the leading-order equations in the asymptotic limit.

It is now determined that the numerical Reynolds number Re_∞ has to scale as one. Following Eq. (2.12), Re_∞ is a function of the μ_∞, and thus n_P. It can be shown using Eq. (2.10) and the definitions of $\tilde{D}$ given in Eq. (2.8) that:

$$\mu_\infty = \frac{\rho_\infty c_\infty^2 u_\infty L}{n_{P,\infty}} \tag{2.16}$$

where $n_{P,\infty}$ is the far-field quantity for the normalization parameter n_P. Substituing Eq. (2.16) into Eq. (2.12) and remembering that the numerical Reynolds number scales as one, it yields:

$$n_{P,\infty} = \rho_\infty c_\infty^2 \tag{2.17}$$

Eq. (2.17) tells us that in the asymptotic limit, the normalization parameter n_P scales as $\rho_\infty c_\infty^2$ which leaves us with two options: either $n_P = \rho c^2$ or $n_P = P$. The choice was made to use $n_P = \rho c^2$ in the asymptotic limit: it was found to behave well and the pressure can become locally negative and null in some particular case as shown in Section 2.5. This normalization parameter is only valid in the asymptotic limit and the purpose of this paper is to define a viscosity coefficient μ that is valid for a wide range of Mach numbers. Thus, it is proposed to define the high-order viscosity coefficient μ_e as follows:

$$\mu_e = h^2 \frac{\max(\tilde{D}_e, J)}{(1 - f(M))\rho c^2 + f(M)\rho||\vec{u}||^2} \tag{2.18}$$

where $f(M)$ is a function of the local Mach number M with the following properties:

$$\begin{cases} f(M) \to 0 \text{ as } M \to 0 \\ f(M) \to 1 \text{ as } M \geq 1 \end{cases} \quad (2.19)$$

The choice of the function $f(M)$ is not fixed and a few examples are available in the literature. A simple definition is $f(M) = \min(M, 1)$ which meets the conditions of Eq. (2.19). Another definition for $f(M)$ was proposed by [?]. All of the numerical results presented in Section 2.5 were obtained by using $f(M) = \min(M, 1)$ which is simple to implement. A convergence test for a subsonic flow over a 2-D cylinder will show that this definition of $f(M)$ yields the correct behavior in the asymptotic limit. The definition of the high-order viscosity coefficient $\mu_e(\vec{r}, t)$ should behave well for complex flow where a near incompressible regime coexists with a supersonic flow domain since $f(M)$ is function of the local Mach number.

For clarity purpose, the full definition of the viscosity coefficient $\mu(\vec{r}, t)$ is recalled:

$$\begin{cases} \mu(\vec{r}, t) = \max(\mu_{max}(\vec{r}, t), \mu_e(\vec{r}, t)) \\ \text{where } \mu_{max}(\vec{r}, t) = \frac{h}{2}(||\vec{u}|| + c) \\ \text{and } \mu_e(\vec{r}, t) = h^2 \frac{\max(\tilde{D}_e, J)}{(1-f(M))\rho c^2 + f(M)\rho||\vec{u}||^2} \\ \mu(\vec{r}, t) = \kappa(\vec{r}, t) \end{cases} \quad (2.20)$$

These viscosity coefficients are valid for both the multi-D Euler equations with variable and constant area and are employed with the dissipative terms detailed in Eq. (2.12). The reader will notice that, through the derivation, none assumption was made on the type of equation of state besides the convexity condition on the entropy function s. The remaining of this paper (Section 2.5) will focus on demonstrating that the definition of the viscosity coefficient given in Eq. (2.20) is indeed

well-scaled in the asymptotic limit and that shocks are still well resolved.

2.4 Solution Techniques Spatial and Temporal Discretizations

In order to detail the partial and temporal discretization used for this study, the system of equations Eq. (2.7) is considered under the following form for simplicity:

$$\partial_t U + \vec{\nabla} \cdot F(U) = S \tag{2.21}$$

where U is the vector solution, F is a conservative vector flux and S is a vector source that can contain the non-conservative term $P\vec{\nabla}A$.

2.4.1 Spatial and Temporal Discretizations

The system of equation given in Eq. (3.15) is discretized using a continuous Galerkin finite element method and high-order temporal integrators provided by the MOOSE framework.

2.4.1.1 CFEM

In order to apply the continuous finite element method, Eq. (3.15) is multiplied by a smooth test function ϕ, integrated by part and each integral is split onto each finite element e of the discrete mesh Ω bounded by $\partial\Omega$, to obtain a weak solution:

$$\sum_e \int_e \partial_t U \phi - \sum_e \int_e F(U) \cdot \vec{\nabla}\phi + \int_{\partial\Omega} F(U)\vec{n}\phi - \sum_e \int_e S\phi = 0 \tag{2.22}$$

The integrals over the elements e are evaluated using quadrature-point rules. The Moose framework provides a wide range of test function and quadrature rules: trapezoidal and Gauss rules among others. Linear Lagrange polynomials will be used as test functions and should ensure second-order convergence for smooth functions. The order of convergence will be demonstrated.

The MOOSE framework offers both first- and second-order explicit and implicit temporal integrators. In all of the numerical examples presented in Section 2.5, the time-dependent term $\int_e \partial_t U \phi$ will be evaluated using the second-order temporal integrator BDF2. By considering three solutions, U^{n-1}, U^n and U^{n+1} at three different time t^{n-1}, t^n and t^{n+1}, respectively, it yields:

$$\int_e \partial_t U \phi = \int_e \left(\omega_0 U^{n+1} + \omega_1 U^n + \omega_2 U^{n-1} \right) \phi \qquad (2.23)$$

$$\text{with } \omega_0 = \frac{2\Delta t^{n+1} + \Delta t^n}{\Delta t^{n+1} \left(\Delta t^{n+1} + \Delta t^n \right)},$$

$$\omega_1 = -\frac{\Delta t^{n+1} + \Delta t^n}{\Delta t^{n+1} \Delta t^n}$$

$$\text{and } \omega_2 = \frac{\Delta t^{n+1}}{\Delta t^n \left(\Delta t^{n+1} + \Delta t^n \right)}$$

where $\Delta t^n = t^n - t^{n-1}$ and $\Delta t^{n+1} = t^{n+1} - t^n$.

2.4.2   Boundary conditions

The boundary conditions will be treated by either using Dirichlet or Neumann conditions. The multi-D Euler equations are wave-dominated systems that require great care when dealing with boundary conditions. It is often recommended to use the characteristic equations to compute the correct flux at the boundaries. Our implementation of the subsonic boundary conditions will follow the method described in [16] that was developed for Ideal Gas and Stiffened Gas equation of states. For each numerical solution presented in Section 2.5, the type of boundary conditions used will be specified and taken amping the followings: supersonic inlet, subsonic inlet (stagnation pressure boundary), supersonic outlet and subsonic inlet (static pressure boundary).

2.4.3 Solver

A Free-Jacobian-Newton-Krylov (FJNK) method is used to solve for the solution at each time step. The jacobian matrix of the discretized equations was derived by hand, hard coded and used as a preconditioner. This method requires the partial derivative of the pressure with respect to the conservative variables to be known. The contribution of the artificial dissipative terms to the jacobian matrix is simplified by assuming constant viscosity coefficients as shown in Eq. (2.24) for the dissipative terms of the continuity equation:

$$\frac{\partial}{\partial U_i}\left(\kappa\vec{\nabla}\rho\vec{\nabla}\phi\right) = \kappa\frac{\partial}{\partial U_i}\left(\rho\right)\vec{\nabla}\phi \tag{2.24}$$

where U_i denotes the set of conservative variables.

2.5   Numerical Results

This section is dedicated to presenting 1- and 2-D numerical results obtained by solving Eq. (2.7) with the entropy viscosity method. This section has two objectives: validate our new definition of the viscosity coefficients for the low Mach limit, and, make sure that the new definition can still resolve shocks.

The first set of 1-D simulations consist of liquid water and steam flowing in a convergent-divergent nozzle. This test is interesting for multiple reasons: a steady-state is reached (some stabilization methods are known to have difficulties to reach a steady-state ([?, ?]), it can be performed for liquid and gas phases, and, an analytical solution of the steady-state solution is available which allow for convergence study. The 1-D Leblanc shock tube test [?] (in a straight pipe) is also performed and consists of a flow developing shocks. A convergence study will be performed in order to demonstrate convergence of the numerical solution to the exact solution.

21

This section also included 2-D simulations from subsonic to supersonic flows. Subsonic flows of a gas over a 2-D cylinder and a hump [?] are simulated and results are shown for various far-field Mach numbers. Numerical results of a supersonic flow in a compression corner are provided to illustrate the capabilities of the new definition in the supersonic case. Convergence studies are performed when an analytical solution is available.

For each simulation, informations relative to the boundary conditions and the equation of state will be provided. All of the numerical solution presented in this section are run with the second-order temporal integrator $BDF2$ and linear polynomials test functions. The integrals are numerically computed using a second-order Gauss quadrature rule. The Ideal Gas [?] or Stiffened Gas equation of state [?] are used and a generic formulation is recalled in Eq. (2.25).

$$P = (\gamma - 1)\rho(e - q) - \gamma P_\infty \qquad (2.25)$$

where the parameters q and P_∞ are fluid dependent and will be specified in time. Eq. (2.25) degenerates to the Ideal Gas equation of state by setting q and P_∞ to zero. The Ideal and Stiffened Gas equation of states have a convex entropy s:

$$s = C_v \ln \left(\frac{P + P_\infty}{\rho^{\gamma - 1}} \right)$$

2.5.1 Liquid water in a 1-D divergent-convergent nozzle

The simulation consists of liquid water flowing through a 1-D convergent-divergent nozzle with the following equation, $A(x) = 1 + 0.5\cos(2\pi x/L)$, where $L = 1m$ is the length of the nozzle. At the inlet, the stagnation pressure and temperature are set to $P_0 = 1MPa$ and $T_0 = 453K$, respectively. At the outlet, only the static pressure

22

is specified: $P_s = 0.5MPa$. Details about the theory related to the inlet and outlet boundary conditions can be found in [16]. Initially, the temperature is uniform and set equal to the stagnation temperature and the pressure linearly decreases from the stagnation pressure to the static one. Finally, the liquid is assumed at rest. The Stiffened Gas equation of state is used to model the liquid water with the parameters provided in Table 2.1.

Table 2.1: Stiffened Gas Equation of State parameters for liquid water.

γ	C_v $(J \cdot kg^{-1} \cdot K^{-1})$	P_∞ (Pa)	q $(J \cdot kg^{-1})$
2.35	1816	10^9	-1167.10^3

Because of the low pressure difference between the inlet and the outlet, and the large value of P_∞, the flow remains subsonic and thus, should not display any shock. Enthalpy and entropy are conserved through the nozzle, and these conservation relations are used to determine the exact solution at steady-state [?]. Plots of the velocity, density and pressure are given at steady-state in Fig. 2.1a, Fig. 2.1b, Fig. 2.1c, respectively, along with the exact solution for comparison. The viscosity coefficients are also plotted in Fig. 2.1d. The mesh used is uniform and has 50 cells.
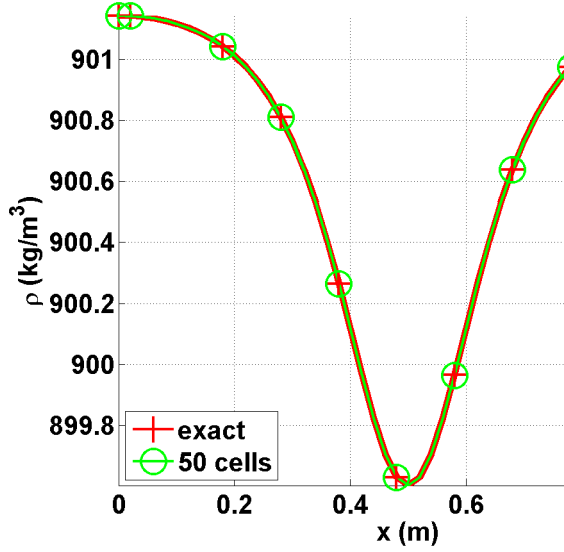
(a) Velocity solution at steady-state.
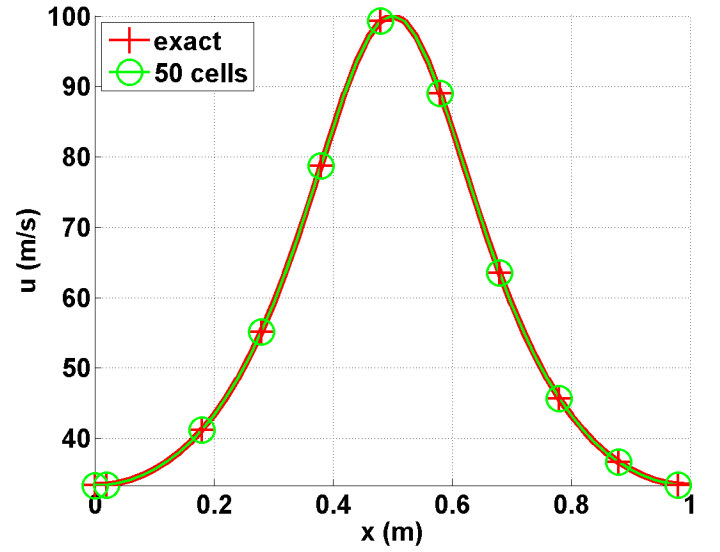
(b) Density solution at steady-state
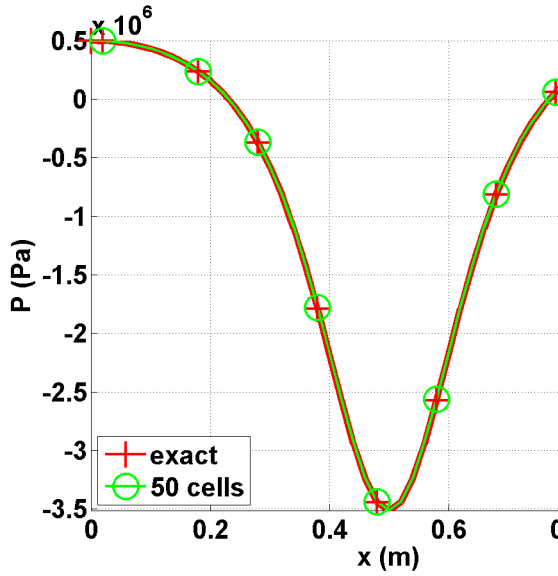
(c) Pressure solution at steady-state.
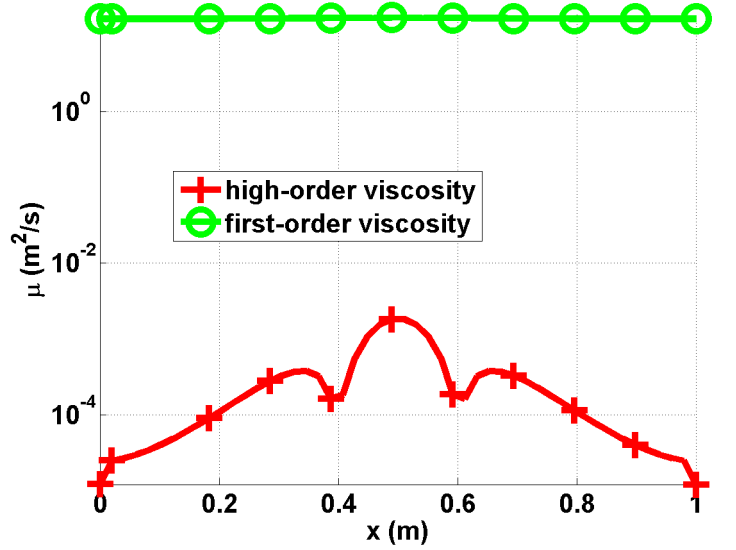
(d) Viscosity coefficients at steady-state.

Figure 2.1: Steady-state solution for liquid phase in a 1-D convergent-divergent nozzle with an uniform mesh of 50 cells.

The numerical and exact solutions of the velocity, pressure and density given in Fig. 2.1 for a fairly coarse mesh (50 cells) perfectly overlap: it is noted that

the numerical solution is symmetric with respect to the nozzle throat located in $x = 0.5m$. The second-order viscosity coefficient is very small compare to the first-order one as expected: (i) the numerical solution is smooth as shown in Fig. 2.1d and (ii) the flow is in a low Mach regime and thus isentropic . A convergence study was performed using the exact solution as a reference: the L1 and L2 norms of the error and the corresponding convergence rates are computed at steady-state on various uniform mesh from 4 to 256 cells. The results for linear polynomials $\mathbb{Q}_1$ are reported in Table 2.2 and Table 2.3 for the primitive variables: density, velocity and pressure.

Table 2.2:   L1 norm of the error for the liquid phase in a 1-D convergent-divergent nozzle at steady-state.

cells	density	rate	pressure	rate	velocity	rate
4	$2.8037 \ 10^{-1}$	–	$8.4705e \ 10^{5}$	–	7.2737	–
8	$1.3343 \ 10^{-1}$	1.0713	$4.7893e \ 10^{5}$	0.24227	6.1493	0.074683
16	$2.9373 \ 10^{-2}$	2.1835	$1.0613e \ 10^{5}$	2.3247	1.2275	2.4501
32	$5.1120 \ 10^{-3}$	2.5225	$1.8446 \ 10^{4}$	2.6959	$1.8943 \ 10^{-1}$	3.0966
64	$1.0558 \ 10^{-3}$	2.2755	$3.7938 \ 10^{3}$	2.3207	$3.7919 \ 10^{-2}$	2.3323
128	$2.3712 \ 10^{-4}$	2.1547	$8.4471 \ 10^{2}$	2.0624	$8.5517 \ 10^{-3}$	2.0473
256	$5.6058 \ 10^{-5}$	2.0806	$1.9839 \ 10^{2}$	2.0478	$2.0475 \ 10^{-3}$	1.9833
512	$1.3278 \ 10^{-5}$	2.0778	46.622	2.0478	$4.9516 \ 10^{-4}$	1.9669

Table 2.3: L2 norm of the error for the liquid phase in a 1-D convergent-divergent nozzle at steady-state.

cells	density	rate	pressure	rate	velocity	rate
4	$3.106397 \ 10^{-1}$	–	$5.254445 \ 10^5$	–	3.288543	–
8	$7.491623 \ 10^{-2}$	2.07	$1.636966 \ 10^5$	1.60	1.823880	0.90
16	$2.079858 \ 10^{-2}$	1.80	$4.627338 \ 10^4$	1.75	$4.990605 \ 10^{-1}$	1.83
32	$5.329627 \ 10^{-3}$	1.90	$1.180287 \ 10^4$	1.92	$1.261018 \ 10^{-1}$	1.93
64	$1.341583 \ 10^{-3}$	1.94	$2.967104 \ 10^3$	1.98	$3.160914 \ 10^{-2}$	1.99
128	$3.359766 \ 10^{-4}$	1.99	$7.428087 \ 10^2$	1.99	$7.907499 \ 10^{-3}$	1.99
256	$8.403859 \ 10^{-5}$	1.99	$1.857861 \ 10^2$	1.99	$1.977292 \ 10^{-3}$	1.99
512	$2.10075 \ 10^{-5}$	1.99	27.048	1.99	$4.9516 \ 10^{-4}$	1.99

It is observed that the convergence rate for the L1 and L2 norm of the error is 2: the entropy viscosity method conserves the high-order accuracy when the numerical solution is smooth, and the new definition of the entropy viscosity coefficient seems to behave as expected in the low Mach limit.

2.5.2   Steam in a 1-D divergent-convergent nozzle

Instead of liquid water, we now simulate a flow of steam using the exact same 1-D geometry, initial conditions and boundary conditions as in Section 2.5.1. The Stiffened gas equation of state is still used but with different parameters that are given in Table 2.4: steam is a gas and compressible effects will become dominant.

Table 2.4: Stiffened Gas Equation of State parameters for steam.

γ	C_v $(J \cdot kg^{-1} \cdot K^{-1})$	P_∞ (Pa)	q $(J \cdot kg^{-1})$
1.43	1040	0	2030.10^3

The pressure difference applied between the inlet and outlet is large enough to make the steam accelerates through the nozzle and result in the formation of shock in the divergent part. The behavior is different from what is observed for the liquid water phase in Section 2.5.1 because of the liquid to gas density ratio that is of 1000. Even though a shock forms, an exact solution at steady-state is still available [?]. The objective of this section is to show that using the new definition of the viscosity coefficient in Eq. (2.20), the shock can be correctly resolved without spurious oscillation. The steady-state numerical solution is shown in Fig. 2.2 and was run with a mesh of 1600 cells.

(a) Velocity solution at steady-state.

(b) Density solution at steady-state

(c) Pressure solution at steady-state.

(d) Viscosity coefficients at steady-state.
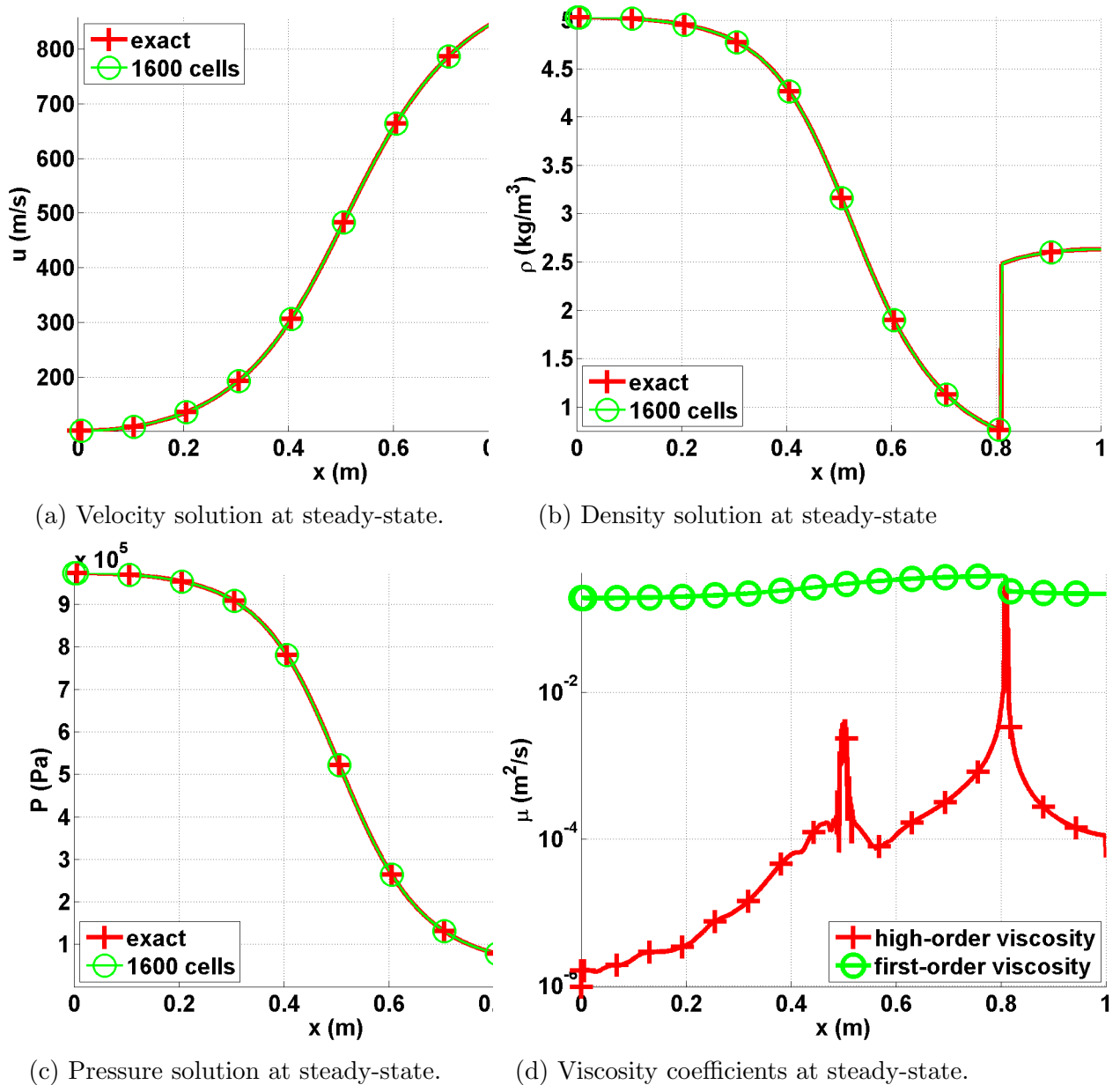
Figure 2.2: Steady-state solution for vapor phase in a 1-D convergent-divergent nozzle.

The steady-state solution of the density, velocity and pressure are given in Fig. 2.2a, Fig. 2.2b and Fig. 2.2c. The steady-solution displays a shock around $x = 0.8m$ and

match the exact solution. In Fig. 2.2d, the first- and second-order viscosity coefficients are log plotted at steady-state: the second-order viscosity coefficient is peaked in the shock region around $x = 0.8m$ as expected, and saturate to the first-order viscosity coefficient. The profile also displays another peak at $x = 0.5m$ that corresponds to the position of the sonic point for a 1-D convergent-divergent nozzle: this particular point is known to develop small instabilities that are detected when computing the jumps of the pressure and density gradients. Anywhere else, the second-order viscosity coefficient is small. In order to prove convergence of the numerical solution to the exact solution, a convergence study is performed. Because of the presence of a shock, second-order accuracy cannot be achieved. However, the convergence rate of a numerical solution containing a shock is known and expected to be of 1 and 1/2 when computing the L1 and L2 norms of the error, respectively (see Theorem 9.3 in [?]). Results are reported in Table 2.5 and Table 2.6 for the primitive variables: density, velocity and pressure.

Table 2.5: L1 norm of the error for the vapor phase in a 1-D convergent-divergent nozzle at steady-state.

cells	density	rate	pressure	rate	velocity	rate
5	$0.72562 \ 10^{-1}$	–	$1.5657 \ 10^5$	–	173.69	–
10	$0.4165 \ 10^{-1}$	0.80088	$9.6741 \ 10^4$	0.63425	120.69	0.52519
20	$0.20675 \ 10^{-1}$	1.0104	$4.9193 \ 10^4$	0.96971	72.149	0.74228
40	$0.093703 \ 10^{-1}$	1.1417	$2.0103 \ 10^4$	0.72728	34.716	1.0554
80	$0.047328 \ 10^{-1}$	0.9854	$1.0208 \ 10^4$	0.9777	16.082	1.1101
160	$0.023965 \ 10^{-2}$	0.9817	$5.1969 \ 10^3$	0.9739	7.9573	1.0150
320	$0.020768 \ 10^{-2}$	0.9886	$2.5116 \ 10^3$	1.0490	3.7812	1.0734
640	$0.0059715 \ 10^{-2}$	1.0160	$1.2754 \ 10^3$	0.9776	1.8353	1.0428

Table 2.6: L2 norm of the error for the vapor phase in a 1-D convergent-divergent nozzle at steady-state.

cells	density	rate	pressure	rate	velocity	rate
5	$9.7144 \ 10^{-1}$	–	$2.0215 \ 10^5$	–	236.94	–
10	$5.9718 \ 10^{-1}$	0.70195	$1.3024 \ 10^5$	0.63425	166.56	0.50854
20	$2.9503 \ 10^{-1}$	1.0173	$6.6503 \ 10^4$	0.96971	103.36	0.68831
40	$1.8193 \ 10^{-1}$	0.69747	$4.0171 \ 10^4$	0.72728	66.374	0.6390
80	$1.3366 \ 10^{-1}$	0.44485	$2.3163 \ 10^4$	0.43576	42.981	0.62692
160	$9.6638 \ 10^{-2}$	0.46790	$1.7263 \ 10^4$	0.42413	31.717	0.43844
320	$7.0896 \ 10^{-2}$	0.44688	$1.2763 \ 10^4$	0.43571	23.138	0.45499
640	$5.2191 \ 10^{-2}$	0.44190	$9.4217 \ 10^3$	0.43790	16.910	0.45238

The convergence rates for the L1 and L2 norms of the error are close to the theoretical values which prove convergence of the numerical solution to the exact solution.

It is also interesting to investigate the effect of the first-order viscosity onto the steady-state solution. In Fig. 2.3, the steady-state velocity profile is plotted when using the first- and second-order viscosity coefficients: the main difference between the two numerical solution is in the resolution of the shock around $x = 0.8m$. The first-order viscosity coefficient is by definition more dissipative and will smooth out the solution. In the other hand, the high-order viscosity better resolves the shock and allow high-order accuracy away from the shock region. It is also noted that the numerical solution obtained with the first-order viscosity coefficient is satisfying: this is due to the nature of the solution that contains a standing shock, and thus,

31

will force the shock to form even with large artificial dissipation.
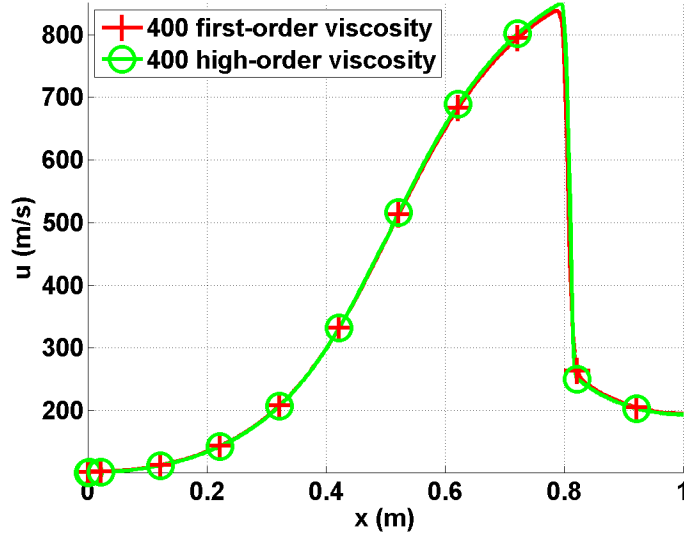
Figure 2.3: Velocity profile at steady-state with the first- and second-order viscosity for a mesh with 400 cells.

2.5.3   Leblanc shock tube

The 1-D Leblanc shock tube is a Riemann problem designed to test the robustness and the accuracy of the stabilization method. The initial conditions are given in Table 2.7. The ideal gas equation of state is used to compute the fluid pressure with the following heat capacity ratio $\gamma = 5/3$.

Table 2.7:   Initial conditions for the 1-D Leblanc shock tube.

	ρ	u	e
left	1.	0.	0.1
right	10^{-3}	0.	10^{-7}

This test is computationally challenging because of the large left to right pressure ratio. The computational domain consists of a 1-D pipe of length $L = 9m$ with an interface located at $x = 2m$. At $t = 0.s$, the interface is removed, allowing the fluid to move. The numerical solution is run until $t = 4.s$ and the density, momentum and total energy profiles are given in Fig. 2.4a, Fig. 2.4b and Fig. 2.4c, respectively, along with the exact solution. The viscosity coefficients are also plotted in Fig. 2.4d. These plots were run with three different uniform mesh of 800, 3200 and 6000 cells and a constant time step $\Delta t = 10^{-3}s$..

(a) Density profile.

(b) Velocity profile.

(c) Pressure profile.

(d) Viscosity coefficients.
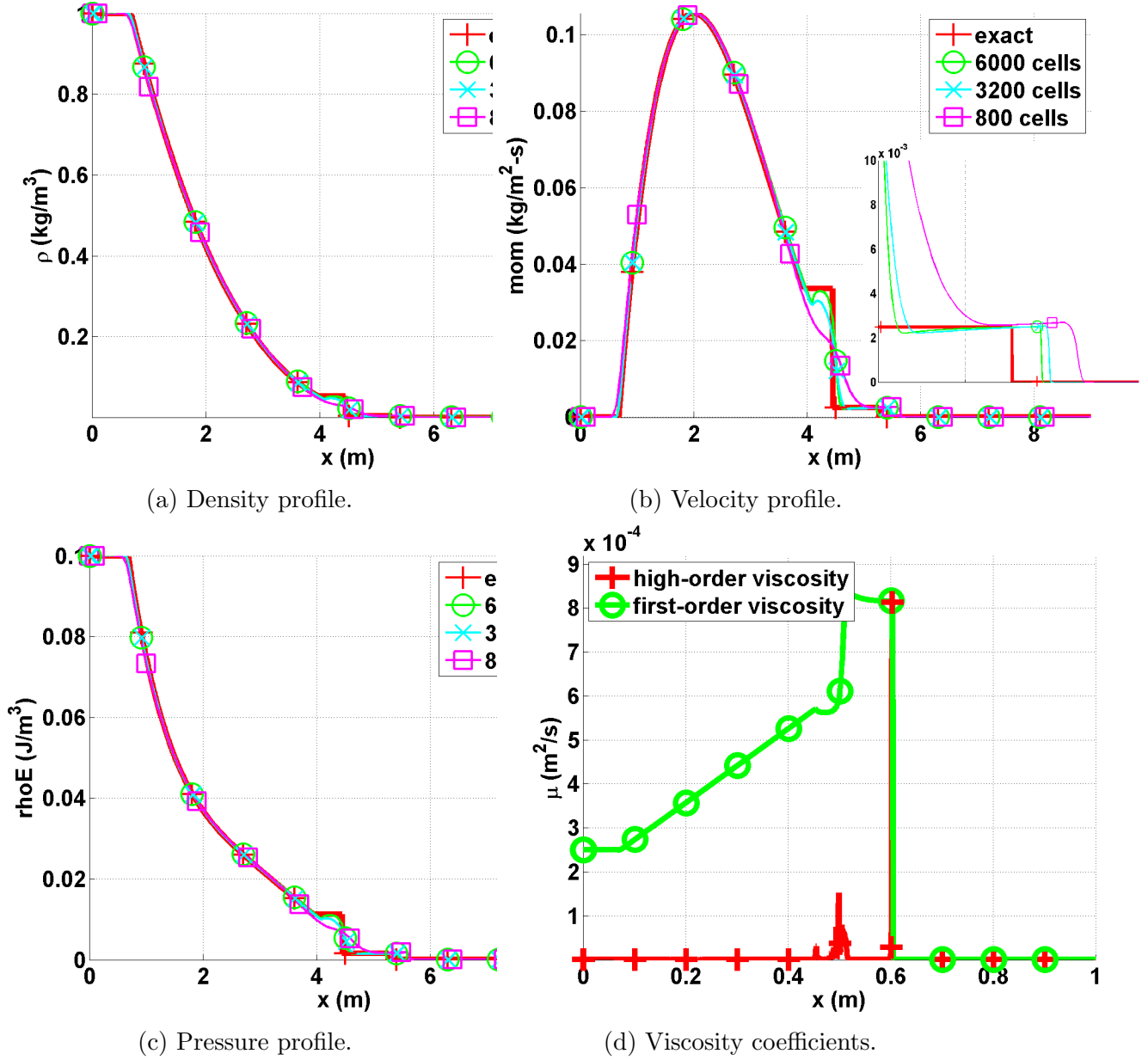
Figure 2.4: Numerical solution for the 1-D Leblanc shock tube at $t = 4.s$.

The density, momentum and total energy profiles given in Fig. 2.4 do not display any oscillations. In Fig. 2.4b, the shock region is zoomed in for better resolution: the shock is well resolved and do not show any oscillation. It is also observed that

the shock position of the numerical solution converges to the exact position when refining the mesh. The contact wave is shown in Fig. 2.4b at $x = 4.5m$. The second-order viscosity coefficient profile is shown in Fig. 2.4d and behaves as expected: it saturates to the first-order viscosity in the shock region and thus prevent oscillations from forming. In the contact wave at $x = 4.5m$, a smaller peak is observed that is due to the presence of the jumps in the definition of the second-order viscosity coefficient (Eq. (2.20)).

Once again, a convergence study is performed in order to prove convergence of the numerical solution to the exact solution. As for the vapor phase in the 1-D nozzle (Section 2.5.2), the expected convergence rate for the L1 and L2 norms of the error are 1 and 1/2, respectively. The exact solution was obtained by running a 1-D Riemann solver and used as a reference solution to compute the L1 and L2-norms of the error that are reported in Table 2.8 and Table 2.9 for the conservative variables: density, momentum and total energy.

Table 2.8: L1 norm of the error for the 1-D Leblanc test at $t = 4.s$.

cells	density	rate	momentum	rate
100	$1.0354722\ 10^{-2}$	–	$3.5471714\ 10^{-3}$	–
200	$7.2680512\ 10^{-3}$	0.51064841	$2.5933119\ 10^{-3}$	0.45187331
400	$5.0825628\ 10^{-3}$	0.51601245	$2.0668092\ 10^{-3}$	0.32739054
800	$3.4025056\ 10^{-3}$	0.57895861	$1.4793838\ 10^{-3}$	0.48240884
1600	$2.1649953\ 10^{-3}$	0.65223363	$9.7152832\ 10^{-4}$	0.6066684
3200	$1.2465433\ 10^{-3}$	0.79643094	$5.5937409\ 10^{-4}$	0.79644263
6400	$6.4476928\ 10^{-4}$	0.95107804	$3.0244198\ 10^{-4}$	0.88715502
12800	$3.3950948\ 10^{-4}$	0.92533116	$1.5958118\ 10^{-4}$	0.9223679

cells	total energy	rate
100	0.0014033046	–
200	$9.8611746\ 10^{-4}$	0.5089968
400	$7.7844421\ 10^{-4}$	0.34116585
800	$5.5702549\ 10^{-4}$	0.48285029
1600	$3.5720171\ 10^{-4}$	0.64100438
3200	$2.0491799\ 10^{-4}$	0.80169235
6400	$1.0914891\ 10^{-4}$	0.90874889
12800	$5.7909794\ 10^{-5}$	0.91441847

Table 2.9:   L2 norm of the error for the 1-D Leblanc test at $t = 4.s$.

cells	density	rate	momentum	rate
100	$5.7187851\ 10^{-3}$	–	$1.7767236\ 10^{-3}$	–
200	$3.8995238\ 10^{-3}$	0.55241073	$1.4913161\ 10^{-3}$	0.25263314
400	$2.8103526\ 10^{-3}$	0.4725468	$1.3305301\ 10^{-3}$	0.164585
800	$2.1081933\ 10^{-3}$	0.41474398	$1.1398931\ 10^{-3}$	0.22310254
1600	$1.5731052\ 10^{-3}$	0.42239201	$9.0394227\ 10^{-4}$	0.33459602
3200	$1.0610667\ 10^{-3}$	0.56809979	$6.2735595\ 10^{-4}$	0.52694639
6400	$7.3309974\ 10^{-4}$	0.53343397	$4.4545754\ 10^{-4}$	0.49399631
12800	$5.1020991\ 10^{-4}$	0.52291857	$3.1266758\ 10^{-4}$	0.5106583

cells	total energy	rate
100	$7.6112265\ 10^{-4}$	–
200	$5.5497308\ 10^{-4}$	0.45571115
400	$4.6063172\ 10^{-4}$	0.26880405
800	$3.7798953\ 10^{-4}$	0.28526749
1600	$2.9584646\ 10^{-4}$	0.35349763
3200	$2.054455\ 10^{-4}$	0.52609289
6400	$1.4670834\ 10^{-4}$	0.48580482
12800	$1.0299897\ 10^{-5}$	0.51032105

The convergence rates are close to the expected values which prove convergence of the numerical solution to the exact solution.

2.5.4 Subsonic flow over a 2-D cylinder

The flow of a fluid over a 2-D cylinder is a typical benchmark case to test the behavior of a numerical method in the low Mach regime. For this test, an analytical solution is available in the incompressible limit or low Mach limit (REFS) and often referred to as potential flow. The main features of the potential flow are the following:

- The solution is symmetric: the iso-mach number lines are used to asses the symmetry of the numerical solution.

- The velocity at the top of the cylinder is twice the incoming velocity set at the inlet.

- The pressure fluctuations are proportional to the inlet Mach number square, as follows:
$$\tilde{P} = \frac{\max(P) - \min(P)}{\max(P)} \propto M_\infty^2$$
where $\tilde{P}$ and M_∞ are the pressure fluctuations and the inlet Mach number, respectively.

The computational domain consists of a 1×1 square with a circular hole of radius 0.05 in its middle. At the inlet, a subsonic stagnation boundary condition is used: the stagnation pressure and temperature are computed using the following relations, valid for the Stiffened and Ideal gas equation of states:

$$\begin{cases} P_0 = P \left(1 + \frac{\gamma-1}{2}M^2\right)^{\frac{\gamma-1}{\gamma}} \\ T_0 = T \left(1 + \frac{\gamma-1}{2}M^2\right) \end{cases} \tag{2.26}$$

The static pressure $P_s = 101325 \, Pa$ is set at the subsonic outlet and a static pressure boundary type is used. The implementation of the pressure boundary conditions is

done on the model of [16]. A solid wall boundary condition is set for the top and bottom walls of the computational domain: the normal velocity is zero since no mass can penetrate the solid body. The mesh is made of triangular cells.

The steady-state for Mach numbers ranging from $M_\infty = 10^{-3}$ to $M_\infty = 10^{-7}$ is shown in Fig. 2.5. The iso-Mach lines are drawn with 50 intervals ranging from 10^{-8} to $2M_\infty$, and allow to assess the symmetry of the numerical solution.
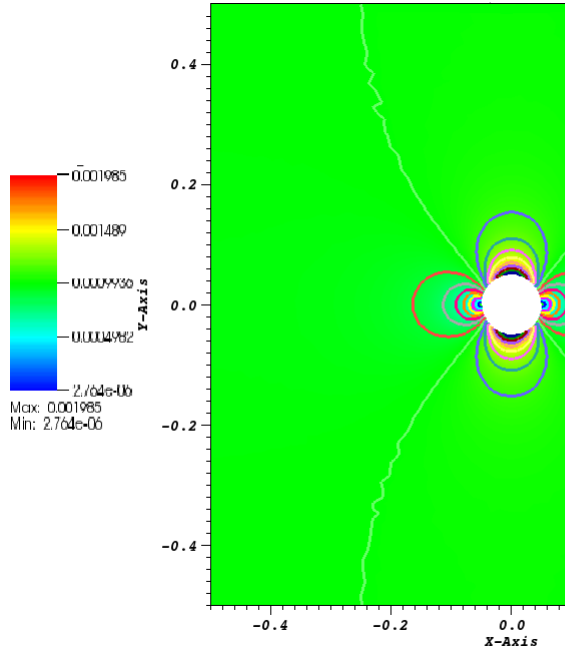
(a) Steady-state solution at $M_\infty = 10^{-3}$.   (b) Steady-state solution at $M_\infty = 10^{-4}$.
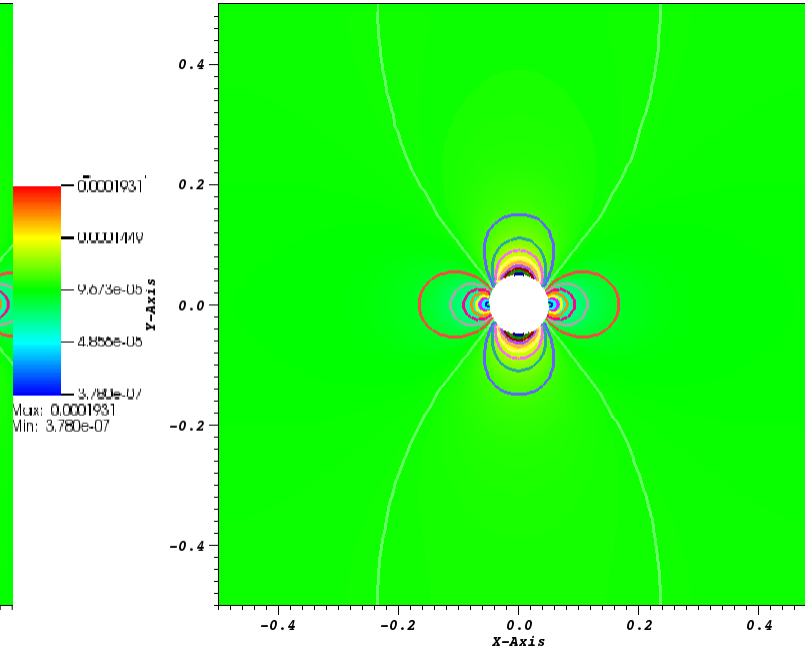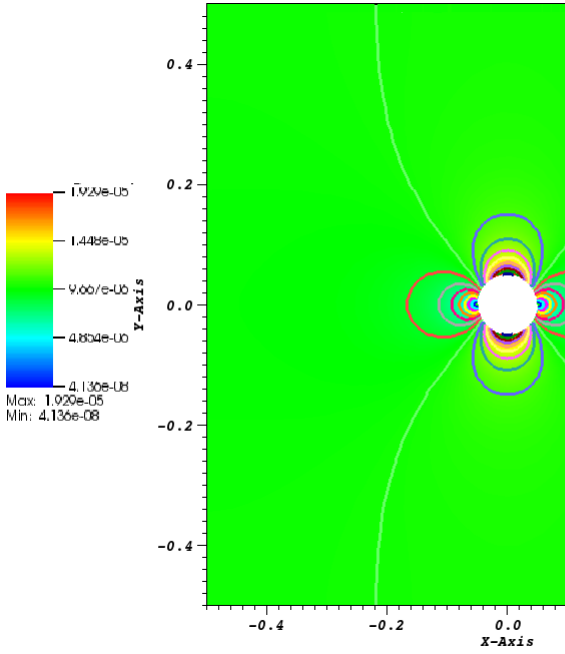
(c) Steady-state solution at $M_\infty = 10^{-5}$.   (d) Steady-state solution at $M_\infty = 10^{-7}$.

Figure 2.5: Steady-state solution for a subsonic flow over a 2-D cylinder.

40

In Table 2.10, the velocity at the top of the cylinder and at the inlet are given for the different values of the Mach number presented in Fig. 2.5. The ratio of the inlet velocity to the velocity at the top of cylinder is also computed and is very close to 2 as expected.

Table 2.10: Velocity ratio for different Mach numbers.

Mach number	inlet velocity	velocity at the top of the cylinder	ratio
10^{-3}	$2.348 \ 10^{-3}$	$1.176 \ 10^{-3}$	1.99
10^{-4}	$2.285 \ 10^{-4}$	$1.145 \ 10^{-4}$	1.99
10^{-5}	$2.283 \ 10^{-5}$	$1.144 \ 10^{-5}$	1.99
10^{-6}	$2.283 \ 10^{-6}$	$1.144 \ 10^{-6}$	1.99
10^{-7}	$2.283 \ 10^{-7}$	$1.144 \ 10^{-7}$	1.99

2.5.5   Subsonic flow over a 2-D hump

This is a another example of an internal flow configuration. It consist of a channel of height $L = 1 \ m$ and length $3L$, with a circular bump of length L and thickness $0.1L$. The bump is located on the bottom wall at a distance L from the inlet. The system is initialized with an uniform pressure $P = 101325 \ Pa$ and temperature $T = 300 \ K$. The initial velocity is computed from the Mach number, M_∞, the pressure, the temperature and the Ideal Gas equation of state with the heat capacity $C_v = 717 \ J/kg - K$ and the heat capacity ratio $\gamma = 1.4$. At the inlet, a subsonic stagnation boun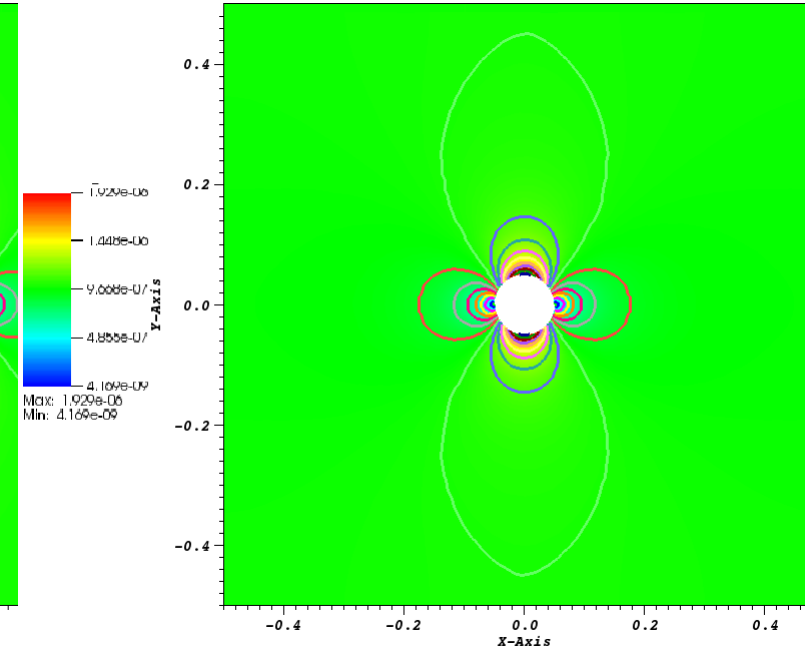dary condition is used and the stagnation pressure and temperature are computed using Eq. (2.26). The static pressure $P_s = 101325 \ Pa$ is set at the

41

subsonic outlet. An uniform grid is used to get the numerical solution until steady-state is reached. The results are shown in Fig. 2.6a, Fig. 2.6b, Fig. 2.6c and Fig. 2.6d for the inlet Mach numbers $M_\infty = 0.7$, $M_\infty = 0.01$, $M_\infty = 10^{-4}$ and $M_\infty = 10^{-7}$, respectively. It is expected that, within the low Mach number range, the solution does not depend on the Mach number and is identical to the solution obtained with an incompressible flow code. On the other hand, for a flow at $M = 0.7$, the compressible effects become more important and shock can form.

(a) Mach 0.7: iso-Mach lines at steady-state.

(b) Mach 10^{-2}: iso-Mach lines at steady-state.

(c) Mach 10^{-5}: iso-Mach lines at steady-state.

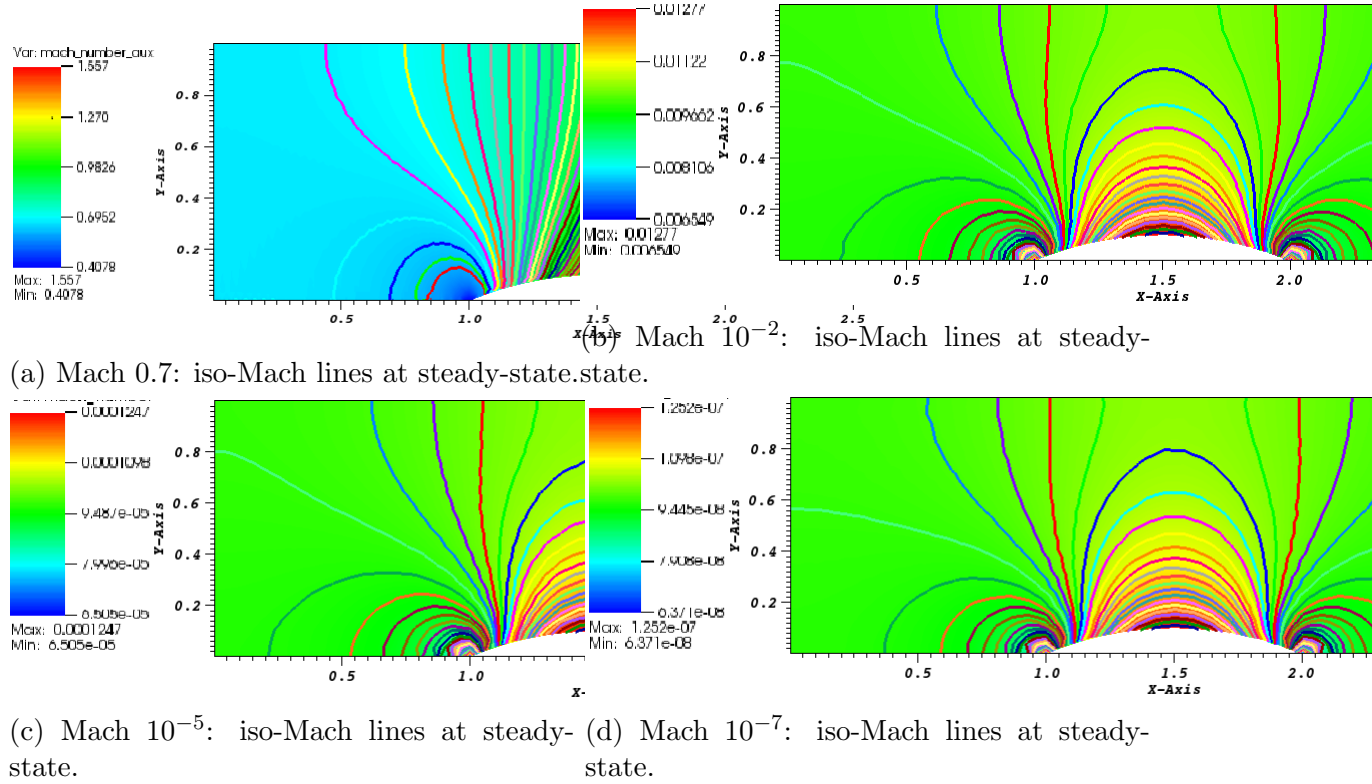(d) Mach 10^{-7}: iso-Mach lines at steady-state.

Figure 2.6: Steady-state solution for a 2-D flow over a circular bump.

The results showed in Fig. 2.6b, Fig. 2.6c and Fig. 2.6d correspond to the low Mach regime. The iso-Mach lines are drawn ranging from the minimum and the

maximum of each legend with 50 intervals. The steady-state solution is symmetric
and does not depend on the value of the inlet Mach number as expected.

In Fig. 2.6a, the steady-state numerical solution develops a shock: the compressibility
effect are no longer negligible. The iso-Mach lines are also plotted with 50 intervals
and ranging from 0.4 to 1.6. The shock is well resolved and does not display any
instability or spurious oscillation.

The results presented in Fig. 2.6 were obtained with the new definition of the viscosity
coefficient (see Eq. (2.20)), and, illustrate the capabilities of the entropy-viscosity
method to adapt to the type of flow (subsonic and transonic flows) without using any
tuning parameters, but by just evaluating the entropy residual that is an indicator
of the entropy production.

2.5.6   Supersonic flow in a compression corner

This is an example of a supersonic flow over a wedge of angle $15°$ where an oblique
shock is generated at steady-state. The Mach number upstream of the shock is fixed
to $M = 2.5$. The initial conditions are uniform: the pressure and temperature are
set to $P = 101325 \ Pa$ and $T = 300 \ K$, respectively. The initial velocity is computed
from the upstream Mach number and using the Ideal Gas equation of state with the
same parameters as in Section 2.5.5. The code is run until steady-state. An analytical
solution for this supersonic flow is available and give the downstream to upstream
pressure, entropy and Mach number ratios [**?**]. The analytical and numerical ratios
are given in see in Table 2.11, and are very close.

Table 2.11: Analytical solution for the supersonic flow on an edge eat 15° at $M = 2.5$.

	analytical downstream to upstream ratio	numerical downstream to upstream ratio
Pressure	2.47	2.467
Mach number	0.74	0.741
Entropy	1.03	1.026

The inlet is supersonic and therefore, the pressure, temperature and velocity are specified using Dirichlet boundary conditions. The outlet is also supersonic and none of the characteristics enter the domain through this boundary: the values will be computed by the implicit solver.
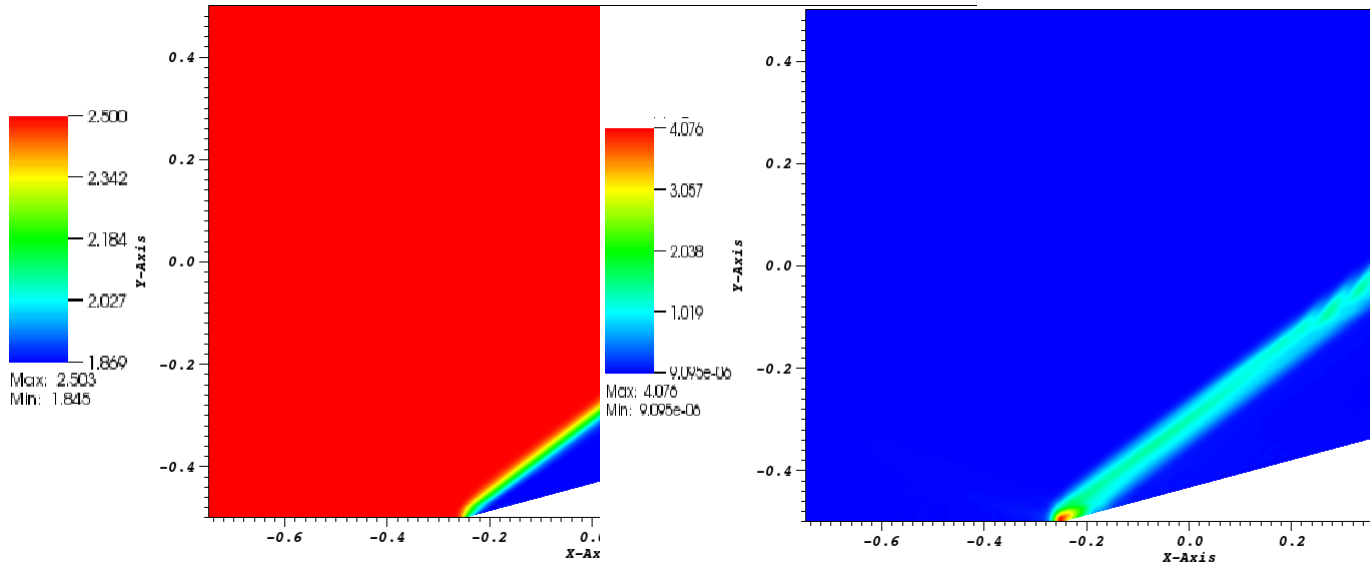
(a) Mach solution at steady-state.

(b) Viscosity coefficient at steady-state.
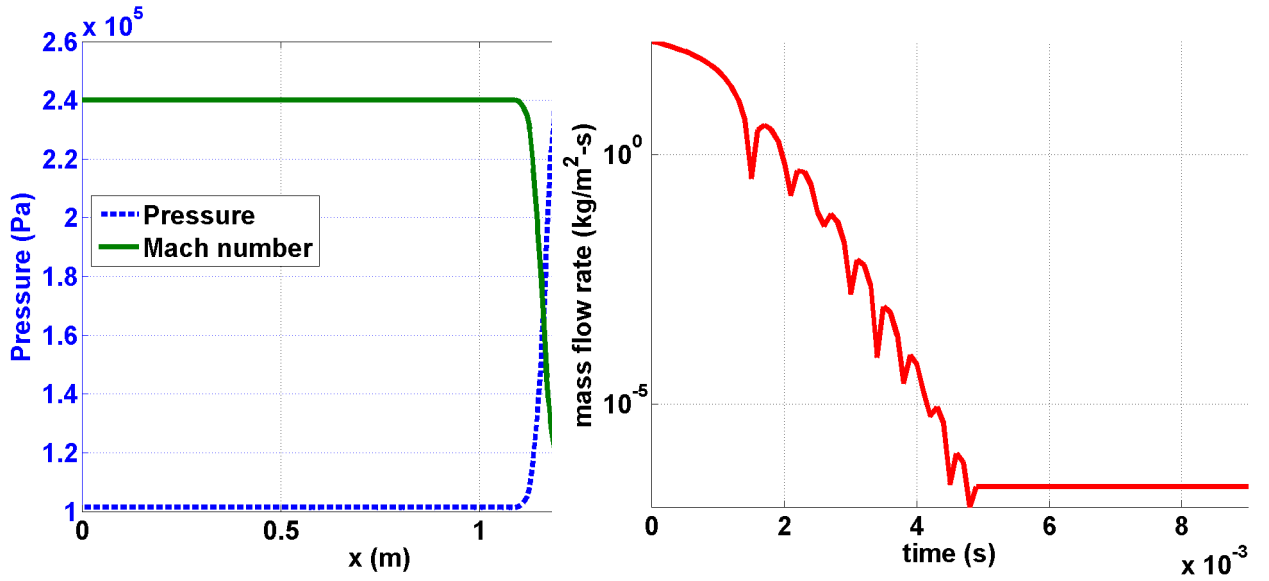
(c) Pressure and Mach number profiles at steady-state

(d) Difference between inlet and outlet mass flow rates as a function of time.

Figure 2.7: Steady-state solution for a flow in a 2-D compression corner.

The steady-state numerical solution is given in Fig. 2.7: the Mach number, the viscosity coefficients are plotted in Fig. 2.7a and Fig. 2.7b, respectively. The steady-

state solution is formed of two regions of constant states, separated by the oblique shock. In Fig. 2.7b, the viscosity coefficient is large in the shock, small anywhere else, and thus, behaves as expected. At the corner of the edge at $x = -0.25\ m$, the viscosity coefficient is peaked because of the treatment of the wall boundary condition: at this particular node, the normal is not well defined and can cause numerical errors. The 1-D plots of the pressure and the mach number at $y = 0$, are also given in Fig. 2.7c: the shock does not show any spurious oscillations and is well resolved. Finally, the difference between the inlet and outlet mass flow rates is plotted in Fig. 2.7d and show that the steady-state is reached.

Overall, the numerical solution does not show any oscillations, match the analytical solution, and the shock is well resolved.

2.6 Conclusions

A new version of the entropy viscosity method valid for a wide range of Mach number and applied to the multi-D Euler equations with variable area was derived and presented. The definition of the viscosity coefficient is now consistent with the low Mach asymptotic limit, does not require an analytical expression of the entropy function, and thus, could be used with any equation of state having a convex entropy. Tests were performed with the Ideal and Stiffened Gas equation of states. In 1-D, convergence of the numerical solution (either smooth or with shocks) to the exact solution was demonstrated by computing the convergence rates of the L1 and L2 norms of the error for flows in convergence-divergent nozzle and a straight pipe. 2-D simulations were also performed for both subsonic and supersonic flows, and various geometries: the entropy viscosity method behaves well for a wide range of Mach number. The numerical results obtained for a flow over a circular bump (subsonic and transonic flows) illustrates the capabilities of the method to adapt to the flow

type.

As future work, the entropy viscosity method will be extended to the 1-D seven equations model [16]. This two-phase flow system of equations is a good candidate for two reasons: it is unconditionally hyperbolic and degenerates to the multi-D Euler equations when one phase disappears.

3. LITERATURE REVIEW: THE IMPORTANCE OF RESEARCH PART TWO- THIS IS DESIGNED TO TEST LONG TITLES IN THE TOC

Text goes here.

3.1   Introduction

Solving the radiation hydrodynamic equations is a challenging task for multiple reasons. First, the characteristic time scales between the radiation and hydrodynamics are different by several orders of magnitude which often requires the radiation part to be solved implicitly to ensure stability. Second, as with any wave-dominated problems, high resolution schemes are needed to accurately resolve shocks. Third, achieving high-order accuracy is challenging but some recent developments provided high-order accuracy results both in time and space when discretizing either the Euler equations [6, 8, 9, 7] or the radiation equation independently from each other.

Significant effort has been put into developing Riemann solvers for both the radiation and hydrodynamic equations. Balsara [2] developed a Riemann solver for the radiation-hydrodynamic equations by considering the frozen approximation that decouples the two physics components. However, such an approach may be questionable in the equilibrium diffusion limit. In this case, the coupling terms drive the physics and have to be accounted for. A *generalized Riemann solver* that accounts exactly for the relaxation terms was developed in [2]. Another approach assumes the strong equilibrium diffusion limit in which radiation diffusion is negligible and the radiation simply advects at the material velocity [4]. In this limit, the radiation hydrodynamics equation can be expressed in the form of the Euler equations with a radiation-modified equation of state (REOS) . Any solution technique for the Euler equations may be applied to these equations. Thus, one may develop approximate

Riemann solvers for these equations and applied them in a general context.

Edwards and al. [10] proposed a two-stage semi-implicit IMEX scheme to solve the coupled radiation-hydrodynamic equations. They applied a Trapezoidal/BDF2 temporal discretization scheme to the nonlinear grey radiation diffusion. The radiation and hydrodynamic equations are solved implicitly and explicitly, respectively. A Riemann solver along with a flux limiter is used to resolve shocks and other waves. Their results show good agreement with semi-analytical solutions.

In this article we propose to solve the 1-D radiation-hydrodynamics equations by using *the entropy viscosity method*. This technique, developed by Guermond et al. for hyperbolic systems of equations [8, 9], consists in adding appropriate dissipative terms to the governing equations. The viscosity coefficient of these terms is modulated by the local entropy production. These dissipative terms are devised to stabilize the numerical scheme and to remove the non-physical oscillations appearing at the shock locations. Generally speaking, entropy is produced at shocks [19]. Thus, by setting the viscosity coefficient proportional to the entropy production, shocks can be detected and tracked and an adequate amount of viscosity is added locally to stabilize the numerical scheme. The entropy production is computed on the fly, by analyzing the entropy residual. This residual is strongly peaked in shocks and small elsewhere. The entropy viscosity method was shown to achieve high-order accuracy away from the shock regions, was successfully applied to non-linear hyperbolic equations using various discretization methods (finite volume, continuous and discontinuous finite elements, spectral method) and yielded high-order accuracy on non-uniform meshes and complex geometries [9, 20]. Because of the similarity between Euler equations and the radiation hydrodynamic equations, it is conjectured that the entropy viscosity method may be a good candidate for resolving shocks occurring in radiation-hydrodynamic phenomena.

The 1-D grey radiation-hydrodynamic (GRH) equations are recalled in Eq. (3.1):

$$\begin{cases} \partial_t (\rho) + \partial_x (\rho u) = 0 \\ \partial_t (\rho u) + \partial_x \left(\rho u^2 + P + \frac{\epsilon}{3}\right) = 0 \\ \partial_t (\rho E) + \partial_x \left[u (\rho E + P)\right] = -\frac{u}{3}\partial_x \epsilon - \sigma_a c \left(aT^4 - \epsilon\right) \\ \partial_t \epsilon + \frac{4}{3}\partial_x (u\epsilon) = \frac{u}{3}\partial_x \epsilon + \partial_x \left(\frac{c}{3\sigma_t}\partial_x \epsilon\right) + \sigma_a c \left(aT^4 - \epsilon\right) \end{cases}, \qquad (3.1)$$

where ρ, u, E, ϵ, P and T are the material density, material velocity, material specific total energy, radiation energy density, material pressure and temperature, respectively. The total and absorption cross sections, σ_t and σ_a, are either constant or density- and temperature-dependent. The variables a and c are the Boltzman constant and the speed of light, respectively. Lastly, the symbols ∂_t and ∂_x denote the temporal and spatial partial derivatives, respectively. The material temperature and pressure are computed with the Ideal Gas equation of state (IGEOS):

$$\begin{cases} P = (\gamma - 1)C_v \rho T \\ e = C_v T \end{cases}, \qquad (3.2)$$

where e is the specific internal energy and is obtained from the expression $e = E - 0.5u^2$. The heat capacity C_v and the heat ratio coefficient γ are assumed constant.

The objective of this paper is to extend the entropy-based viscosity method to the 1-D grey radiation-hydrodynamic equations. The approach followed in this paper is similar to those of [2, 17]: an infinite opacity is assumed and the relaxation terms are ignored in order to make Eq. (3.1) hyperbolic. Then, an entropy equation is derived and used to obtain the functional forms of the viscous stabilization terms. Definitions for the viscosity coefficients are provided.

This paper is organized as follows. In Section 3.2, the entropy viscosity method is

extended to the grey radiation-hydrodynamic equations; details regarding the derivation of the adequate dissipative terms and definitions for the new viscosity coefficients are provided. Spatial and temporal discretization schemes are discussed in Section 3.3 along with the solution algorithm employed to solve the discretized equations. Numerical results are presented in Section 3.4 where the second-order accuracy of the scheme is demonstrated in both the equilibrium diffusion and streaming limits, using the method of manufactured solutions applied to the GRH equations. Then, several numerical test cases, taken from the published literature, are provided; in these simulations, the Mach number varies from 1.05 to 50 [15]. Conclusions are presented in Section 3.5.

3.2 The entropy-based viscosity method applied to the 1-D Radiation-Hydrodynamic equations

In this section, we extend the entropy viscosity method [8, 9, 20] to the 1-D radiation-hydrodynamic equations in a staged process. First, the reader is guided through the main steps that lead to the derivation of the dissipative terms, using the entropy minimum principle [18]. Then, a definition for the entropy viscosity coefficient based upon the entropy production is given.

We recall that the entropy viscosity method was developed for hyperbolic system of equations. However, the radiation hydrodynamic equations are not strictly hyperbolic but several numerical techniques are based on the study of their hyperbolic parts [2, 17]. Thus, following the same rationale, the system of equations given in Eq. (3.1) is made hyperbolic by assuming an infinite opacity (the frozen approximation) and by ignoring the relaxation terms. These two assumptions yield the

following system of equations:

$$
\begin{cases}
\partial_t \left(\rho \right) + \partial_x \left(\rho u \right) = 0 \\
\partial_t \left(\rho u \right) + \partial_x \left(\rho u^2 + P + \frac{\epsilon}{3} \right) = 0 \\
\partial_t \left(\rho E \right) + \partial_x \left[u \left(\rho E + P \right) \right] = -\frac{u}{3} \partial_x \epsilon \\
\partial_t \epsilon + \frac{4}{3} \partial_x \left(u \epsilon \right) = \frac{u}{3} \partial_x \epsilon
\end{cases}
. \tag{3.3}
$$

The jacobian matrix of the hyperbolic terms can be computed to derive the eigen-values:

$$
\lambda_1 = u - c_m, \ \lambda_{2,3} = u \ \text{and} \ \lambda_4 = u + c_m, \tag{3.4}
$$

where c_m is the radiation-modified material speed of sound and is defined as follows:

$$
c_m^2 = \underbrace{P_\rho + \frac{P}{\rho^2} P_e}_{c_{Euler}^2} + \frac{4\epsilon}{9\rho} \tag{3.5}
$$

with P_x the standard shorthand notation for $\partial_x P$, and c_{Euler}^2 denotes the definition of the speed of sound when considering only the 1-D Euler equations. The above hyperbolic system of equations can be recast in a conservative form. This allows us to assume the existence of an entropy function s [13] that depends upon the internal energy e, the density ρ, and the radiation energy density ϵ. Following some algebra given in Appendix ??, an equation satisfied by the entropy s is obtained:

$$
\rho \frac{ds}{dt} = \rho \left(\partial_t s + u \partial_x s \right) = 0, \tag{3.6}
$$

where $\frac{d \cdot}{dt}$ denotes the total or material derivative. Eq. (3.6) is often referred as the entropy residual and is used to prove the entropy minimum principle, $\frac{ds}{dt} \geq 0$, [18].

When adding dissipative terms to each equation of Eq. (3.3) as required in the

entropy viscosity method, the entropy residual equation is modified and some additional terms will appear in the right-hand side of Eq. (3.6). The sign of these extra terms needs to be studied for the entropy minimum principle to hold. As such, the entropy minimum principle is invoked to guide in the derivation of appropriate expressions for each of the dissipative terms. Obtaining the final expression of the dissipative terms is a lengthy process and only the final result along with the key assumptions are stated here. The reader is referred to Appendix ?? for the details of the derivation. The system of equations with the dissipative terms is as follows:

$$
\begin{cases}
\partial_t\left(\rho\right) + \partial_x\left(\rho u\right) = \partial_x\left(\kappa\partial_x\rho\right) \\
\partial_t\left(\rho u\right) + \partial_x\left(\rho u^2 + P + \frac{\epsilon}{3}\right) = \partial_x\left(\kappa\partial_x\rho u\right) \\
\partial_t\left(\rho E\right) + \partial_x\left[u\left(\rho E + P\right)\right] + \frac{u}{3}\partial_x\epsilon = \partial_x\left(\kappa\partial_x(\rho E)\right) \\
\partial_t\epsilon + \frac{4}{3}\partial_x\left(u\epsilon\right) - \frac{u}{3}\partial_x\epsilon = \partial_x\left(\kappa\partial_x\epsilon\right)
\end{cases}
, \qquad (3.7)
$$

where κ is a locally defined positive viscosity coefficient. It was assumed that the following conditions hold:

$$
\begin{cases}
P\frac{\partial s}{\partial e} + \rho^2\frac{\partial s}{\partial\rho} + \frac{4}{3}\rho\epsilon\frac{\partial s}{\partial\epsilon} = 0 \\
s(\rho, e, \epsilon) = \hat{s}(\rho, e) + \frac{\rho_0}{\rho}\tilde{s}(\epsilon)
\end{cases}
\qquad (3.8)
$$

where $-\tilde{s}$ is convex with respect to the radiation energy density ϵ and $-\hat{s}$ is convex with respect to the internal energy e and the specific volume ρ^{-1}. The constant ρ_0 is of order one and appears only for dimensionality purposes.

Once the dissipative terms are obtained, it remains to define the local viscosity coefficient $\kappa(x, t)$. We require the following to hold in the prescription for κ:

- Since the entropy residual is a measure of the entropy production that occurs in shock regions, it is natural to define a viscosity coefficient proportional to

the entropy residual. This will enable shock detection and tracking and will also provide a measure of the viscosity required to stabilize the scheme. This viscosity coefficient is referred to as the *entropy viscosity coefficient* or *second-order viscosity coefficient* and is denoted by $\kappa_e(x, t)$.

- An upper bound on κ is to be set since entropy production can be very large in shocks. For explicit time integration, the maximum value of the viscosity coefficient is related to the Courant-Friedrichs-Lewy number (CFL). The upper bound on κ is defined by analogy to the standard upwind (Godunov) scheme that is known to efficiently smooth out oscillations (but is only first-order accurate). With implicit temporal integrators, the same reasoning is used even if the CFL number may not need to be strictly respected. This upper bound will be referred to as the *first-order viscosity*, denoted by $\kappa_{max}(x, t)$.

- The viscosity coefficient κ that is actually used in the dissipative terms of Eq. (3.3) is defined as follows: $\kappa(x, t) = \min(\kappa_e(x, t), \kappa_{max}(x, t))$. With such a definition, the viscosity added to the system of equations will saturate to the first order viscosity in the shock regions. Elsewhere, the entropy production and thus the viscosity coefficient κ are expected to be small.

Next, we define the local first- and second-order viscosity coefficients $\kappa_{max}(x, t)$ and $\kappa_e(x, t)$, respectively. Following the work of Zingan et al. [20], the first-order viscosity definition is based on the local largest eigenvalue that is known to be $|u| + c_m$ in 1-D:

$$\kappa_{max} = \frac{h}{2} \left(|u| + c_m \right) \tag{3.9}$$

where h is the local grid size. This definition is derived based on the upwind scheme and a simple derivation can be found in [8] in the case of a scalar hyperbolic equation.

Through the definition of the radiation-modified speed of sound c_m, both the material and radiation properties are accounted for in the definition of the first-order viscosity coefficient.

The definition of the second order viscosity coefficient $\kappa_e(x, t)$ is based upon the entropy residual (Eq. (3.6)) recast as a function of pressure P, density ρ and radiation energy density ϵ:

$$\tilde{D}_e(x, t) = \frac{s_e}{P_e} \underbrace{\left(\frac{dP}{dt} - c_{Euler}^2 \frac{d\rho}{dt} \right)}_{\hat{D}_e(x, t)} \tag{3.10}$$

The term s_e is the inverse of the material temperature (Appendix **??**) and P_e is computed from the IGEOS. These two terms are positive so that the sign of the entropy residual $\tilde{D}_e(x, t)$ can be determined by simply inspecting the terms inside the parentheses, denoted by $\hat{D}_e(x, t)$. Such an expression is easier to compute than the one given in Eq. (3.6) which required an analytical expression for the entropy function. In addition to the entropy residual, inter-element jumps in the pressure and density gradients, J, are also accounted for. The objective is to be able to also detect discontinuities that are not shocks, such as contact waves (there is no entropy production in a contact wave), in order to stabilize them as well.

Thus, the entropy viscosity coefficient $\kappa_e(x, t)$ is set to be proportional to $\hat{D}_e(x, t)$ and J with the following form:

$$\kappa_e(x, t) = h^2 \frac{\max(|\hat{D}_e(x, t)|, J)}{n_P} \tag{3.11}$$

where $J = \max_i(J(x_i, t))$, and $J(x_i, t)$ is the jump of a given quantity at cell interface x_i, and n_P is a normalization function (of the same units as pressure) that has to be chosen so that the viscosity coefficient κ has units of m^2/s. The following definition for the normalization function has been chosen: $n_P = \rho c_m^2$. Thus, the final definition

for the viscosity coefficient κ is the following:

$$\kappa_e(x,t) = h^2 \frac{\max(|\hat{D}_e(x,t)|, J)}{\rho c_m^2} \tag{3.12}$$

The jump J in the definition of $\kappa(x,t)$ is piecewise-constant. Its definition is discretization-dependent and defined as follows for Continuous Galerkin FEM:

$$\begin{cases} J_P(x_i,t) = |u|[[\partial_x P]] \\ J_\rho(x_i,t) = c_m^2 |u|[[\partial_x \rho]] \\ J(x_i,t) = \max(J_\rho(x_i,t), J_P(x_i,t)) \end{cases} \tag{3.13}$$

The symbol $[[\cdot]]$ denotes the jump at the cell interface.

The entropy viscosity method is now well defined for the hyperbolic system given in Eq. (3.3) and will be used to solve for the grey radiation-hydrodynamic equations given in Eq. (3.1). However, one may question how the relaxation source terms, $\sigma_a c(aT^4 - \epsilon)$ and the physical diffusion term, $\partial_x(D\partial_x \epsilon)$, may affect the entropy viscosity method. When applying the entropy viscosity method, the radiation energy density equation will now contain a diffusive term and a numerical dissipative term with a vanishing viscosity coefficient κ. As long as the diffusive coefficient $D = \frac{c}{3\sigma_t}$ is larger than the viscosity coefficient κ, the numerical dissipative term should not be required. A way to ensure consistency and prevent the formation of oscillations in the frozen limit is to merge the two second-order derivative terms into one as follows:

$$\partial_x \left(\frac{c}{3\sigma_t} \partial_x \epsilon \right) + \partial_x (\kappa \partial_x \epsilon) \implies \partial_x \left[\max \left(\frac{c}{3\sigma_t}, \kappa \right) \partial_x \epsilon \right] \tag{3.14}$$

Thus, as long as the artificial viscosity coefficient κ is locally smaller that the physical diffusive coefficient $D = \frac{c}{3\sigma_t}$, no artificial viscosity is required to ensure stability of

the numerical scheme. As the diffusive coefficient D goes to zero, shocks can form in the radiation energy density profile and will require a certain amount of viscosity in order to prevent oscillations from appearing.

The effect of the relaxation source terms onto the entropy viscosity method can become problematic in the equilibrium diffusion limit ($\sigma_a c \rightarrow \infty$): the relaxation source terms behave as dissipative terms and make the system parabolic [7]. In [11], a study on the impact of various artificial viscosity methods onto hyperbolic systems with relaxation terms was carried out. It was shown that high-order viscosity coefficients are more suitable since they do not alter the physical solution as much as first-order viscosity terms (upwind scheme). A manufactured solution is employed in Section 3.4.1 to test the convergence of the numerical solution in the equilibrium-diffusion limit. The normalization factor has to be larger than h in order to conserve high-order accuracy.

The reader will notice that, except for the definition of the jumps, the whole method is independent of the spatial discretization employed. The technique could be used with discontinuous Galerkin finite element or finite volume methods. In both cases, an adequate definition of the jump terms can be found in [20].

3.3 Numerical scheme and solution technique

The 1-D radiation-hydrodynamic equations Eq. (3.1) are discretized with the continuous Galerkin finite element method (CGFEM) under the MOOSE framework [3]. To obtain a weak form, the following generic form of Eq. (3.1) is considered:

$$\partial_t U + \partial_x F(U) = S + \partial_x H(U) \tag{3.15}$$

where U is the solution vector, F is a conservative vector flux, S is a vector containing the relaxation source terms and non-conservative terms, and H is the artificial

viscosity dissipative flux:

$$
U = \begin{bmatrix} \rho \\ \rho u \\ \rho E \\ \epsilon \end{bmatrix}, \ F(U) = \begin{bmatrix} \rho u \\ \rho u^2 + P + \frac{\epsilon}{3} \\ u\left(\rho E + P\right) \\ \frac{4}{3}u\epsilon \end{bmatrix}, \ S = \begin{bmatrix} 0 \\ 0 \\ -\frac{u}{3}\partial_x\epsilon - \sigma_a c\left(aT^4 - \epsilon\right) \\ \frac{u}{3}\partial_x\epsilon + \partial_x\left(\frac{c}{3\sigma_t}\partial_x\epsilon\right) + \sigma_a c\left(aT^4 - \epsilon\right) \end{bmatrix},
$$

$$
\text{and } H(U) = \begin{bmatrix} \kappa\partial_x\rho \\ \kappa\partial_x(\rho u) \\ \kappa\partial_x\left(\rho e\right) + \frac{u^2}{2}\kappa\partial_x\rho + \rho u\mu\partial_x u \end{bmatrix}
$$

In order to apply the continuous finite element method, Eq. (3.15) is multiplied by a test function ϕ, integrated by parts over the discrete mesh Ω bounded by $\partial\Omega$, to obtain a weak solution:

$$
\sum_e \int_e \partial_t U\phi - \sum_e \int_e F(U)\partial_x\phi + \int_{\partial\Omega} F(U)\mathbf{n}\phi - \sum_e \int_e S\phi + \sum_e \int_e H(U)\partial_x\phi - \int_{\partial\Omega} H(U)\mathbf{n}\phi = 0
$$

$$(3.16)$$

where e represents the cells of Ω and $\mathbf{n}$ is the outward normal vector to the boundary of the computational domain.

The integrals over the elements e are evaluated using third-order Gauss quadrature rules. The time-dependent term will be evaluated using the implicit second-order temporal integrator BDF2 [7]. Only linear test functions are considered in this paper. The integral on $\partial\Omega$ requires computation of the flux $F(U)$ and $H(U)$ on the boundary. It is chosen to treat the boundary for each physics component independently and details will be given in Section 3.4.2 on how to compute $F(U)$. The viscosity dissipative flux $H(U)$ is zero on the boundaries since the viscosity coeffi-

cients κ and μ are set to zero [8, 9, 20].

The Jacobian-Free Newton Krylov method [12] is employed to solve the system for each time step: Newton's and Krylov methods are used for the outer nonlinear and inner linear solves, respectively. The full Jacobian matrix is used as a preconditioner and is computed by finite difference: this is one of the options available in MOOSE and is reasonably efficient for 1-D simulations.

The entropy residual expression is not integrated over the cell volume as it is usually done in the Galerkin finite element method. The variable values and their gradients are available at quadrature points and at different times, and, thus, can be used to evaluate the entropy residual.

3.4   Numerical results

In this section, numerical results using the entropy viscosity method are presented for the dimensional 1-D grey radiation-hydrodynamic equations. First, second-order accuracy of the method is demonstrated using the method of manufactured solution (MMS). Then, results for some standard radiation-hydrodynamic test cases are given.

3.4.1   Space/time accuracy

The same manufactured solution as in [10] is used in order to test both the diffusive and streaming limit solutions in a slab of thickness $L = 2\pi$ cm. The manufactured solutions are composed of trigonometric functions. Periodic boundary conditions are used for all of the variables. The L_2 norm of the error between the numerical and exact solutions are computed for density, momentum, total material energy, and radiation energy density. For each new simulation, the time step is divided by two and the number of spatial degrees of freedom is doubled. With such settings, the error is expected to decrease by a factor 4 if second-order convergence is achieved.

The first manufactured solution is designed to test the equilibrium-diffusion limit. In that case, the radiation energy is in equilibrium with the material temperature and the opacity is large which means that the radiation mean-free path is not resolved but the variation of the solution is resolved. The following exact solution was used:

$$\begin{cases} \rho = \sin(x - t) + 2 \\ u = \cos(x - t) + 2 \\ T = \frac{0.5\gamma(\cos(x-t)+2)}{\sin(x-t)+2} \\ \epsilon = aT^4 \end{cases} . \qquad (3.17)$$

The cross sections σ_a and σ_t are assumed constant and set to the same value 1000 cm^{-1}. The simulation is run until $t = 3$ sh $(1$ $sh = 10^{-8}$ $sec)$. The L_2 error norm along with its ratio between consecutive simulations are given in Table 3.1 for the equilibrium diffusion limit case.

Table 3.1: L$_2$ norms of the error for for the equilibrium diffusion limit case using a manufactured solution.

# of cells	time step size (sh)	ρ	ratio	ρE	ratio
20	10^{-1}	0.590766	NA	1.333774	NA
40	$5\ 10^{-1}$	0.290626	2.03	0.478819	2.79
80	$2.5\ 10^{-2}$	0.0959801	3.021	0.154119	3.11
160	$1.25\ 10^{-2}$	0.02593738	3.70	0.0405175	3.80
320	$6.25\ 10^{-3}$	$6.471444\ 10^{-3}$	4.00	$9.90446\ 10^{-3}$	4.09
640	$3.125\ 10^{-3}$	$1.584158\ 10^{-3}$	4.01	$2.44727\ 10^{-3}$	4.04
# of cells	time step size (sh)	ϵ	ratio	ρu	ratio
20	10^{-1}	0.00650085	NA	0.910998	NA
40	$5\ 10^{-1}$	0.00124983	5.20	0.4090946	2.23
80	$2.5\ 10^{-2}$	0.000262797	4.76	0.125943	3.25
160	$1.25\ 10^{-2}$	$6.17726\ 10^{-5}$	4.25	$3.381042\ 10^{-3}$	3.72
320	$6.25\ 10^{-3}$	$1.509184\ 10^{-5}$	4.09	$8.373657\ 10^{-3}$	4.04
640	$3.125\ 10^{-3}$	$3.72548\ 10^{-6}$	4.05	$2.070538\ 10^{-3}$	4.04

The second manufactured solution is used to test the method in the streaming limit: the radiation streaming dominates the absorption/re-emission term and

evolves at a fast time scale. The exact solution used is as follows :

$$
\begin{cases}
\rho = \sin(x - t) + 2 \\
u = (\sin(x - t) + 2)^{-1} \\
T = 0.5\gamma \\
\epsilon = \sin(x - 1000t) + 2
\end{cases}
\tag{3.18}
$$

For this manufactured solution, the cross sections are still assumed constant and set to the same value $1\ cm^{-1}$. The final time is $t_{final} = 3\ sh$. Once again, the L_2 error norm is given in Table 3.2 for the density, momentum, material total energy and radiation energy density.

Table 3.2: L_2 norms of the error for for the streaming limit case using a manufactured solution.

# of cells	time step size (sh)	ρ	ratio	$\rho\mathbf{E}$	ratio
20	10^{-1}	$1.4373\ 10^{-2}$	NA	$5.88521\ 10^{-1}$	NA
40	$5.\ 10^{-2}$	$3.760208\ 10^{-3}$	3.82	$1.4244\ 10^{-1}$	4.13
80	$2.5\ 10^{-2}$	$9.91724\ 10^{-4}$	3.79	$3.2047\ 10^{-2}$	4.44
160	$1.25\ 10^{-2}$	$2.4455\ 10^{-4}$	4.06	$7.4886\ 10^{-3}$	4.28
320	$6.25\ 10^{-3}$	$6.280715\ 10^{-5}$	3.89	$1.82327\ 10^{-3}$	4.11
640	$3.125\ 10^{-3}$	$1.57920\ 10^{-5}$	3.98	$4.50463\ 10^{-4}$	4.05
1280	$1.5625\ 10^{-4}$	$3.96096\ 10^{-6}$	3.99	$1.12061\ 10^{-4}$	4.02
# of cells	time step size (sh)	ϵ	ratio	$\rho\mathbf{u}$	ratio
20	10^{-1}	$3.82001\ 10^{-1}$	NA	$2.354671\ 10^{-3}$	NA
40	$5.\ 10^{-2}$	$1.21500\ 10^{-1}$	3.14	$6.138814\ 10^{-4}$	3.84
80	$2.5\ 10^{-2}$	$3.27966\ 10^{-2}$	3.70	$1.74974\ 10^{-4}$	3.51
160	$1.25\ 10^{-2}$	$8.38153\ 10^{-3}$	3.91	$3.61297\ 10^{-5}$	4.84
320	$6.25\ 10^{-3}$	$2.10925\ 10^{-3}$	3.97	$9.03866\ 10^{-6}$	3.99
640	$3.125\ 10^{-3}$	$5.28472\ 10^{-4}$	3.99	$2.25649\ 10^{-6}$	4.01
1280	$1.5625\ 10^{-4}$	$1.322268\ 10^{-4}$	3.99	$5.69984\ 10^{-7}$	3.95

For both manufactured solutions the error is divided by four as the time step and the spatial mesh are reduced by a factor two. Thus, we conclude that GRH equations can be numerically solved with second-order accuracy using the entropy viscosity method when the exact solution is smooth.

3.4.2 Radiation shock simulations

The purpose of this section is to show that the entropy-based viscosity method (Section 3.2) can accurately resolve shocks occurring in radiation-hydrodynamic simulations. Multiple test cases are considered, with Mach numbers of 1.05, 1.2, 2, 5 and 50 [15]. All of the simulations are run with 500 spatial cells and with a Courant-Friedrichs-Lewy (CFL number) of 10 until steady-state (even if the scheme employed here is fully implicit, a CFL number can still be computed and is a good reference for comparison against semi-implicit or fully explicit codes). Linear Lagrange polynomials and the second-order temporal integrator BDF2 are once again used. For clarity, the initial conditions for each test case will be recalled in a table and plots of the density, $\rho(x)$, the radiation temperature, $\theta(x)$, and material temperature, $T(x)$, at steady-state will be given as well as those of the viscosity coefficients, $\kappa(x)$ and $\kappa_{max}(x)$. The computational domain consists of a 1-D slab of thickness L. The initial discontinuity between the left and right states is located at x_0 and will be specified for all test cases. For all of the test cases presented in this paper, the cross sections σ_a and σ_t are assumed constant and set to 853.144 cm^{-1} and 390.711 cm^{-1}, respectively, if not otherwise specified. The heat capacity at constant specific volume is set to $C_v = 0.12348\ jerks/(g - keV)$.

For the Mach 2 simulation, results will also be shown when employing only the first-order viscosity ($\kappa(x,t) = \kappa_{max}(x,t)$) in order to show the benefits of using a high-order viscosity coefficient.

The inlet and outlet boundary conditions (BCs) are given next. The Euler equations and radiation equation are considered independently since the latter one is parabolic. At the inlet, the flow is supersonic and, therefore, no physical information exits the system. Thus, Dirichlet boundary condition can be used. At the outlet,

the flow become subsonic which requires a particular treatment. Following the work from [16], a static boundary condition is implemented. Only the back pressure is provided and the other variables are computed using the characteristic equations. For the radiation equation, vacuum boundary conditions are used at both inlet and outlet.

3.4.2.1 An equilibrium diffusion test

For this test, the inlet Mach number is set to 1.05. The radiation field and material are in equilibrium. The initial conditions are given in Table 3.3. The

Table 3.3: Initial conditions for Mach 1.05.

	left	right
$\rho \ (g/cm^3)$	1.	1.0749588
$u \ (cm/sh)$	0.1228902	0.1144127
$T \ (keV)$	0.1	0.1049454
$\epsilon \ (jerks/cm^3)$	1.372 10^{-6}	1.6642117 10^{-6}

computational domain is of size $L = 0.08 \ cm$ and the initial step is at $x_0 = 0.015$ cm. The numerical solutions at steady state are given in Fig. 3.1, Fig. 3.2 and Fig. 3.3.
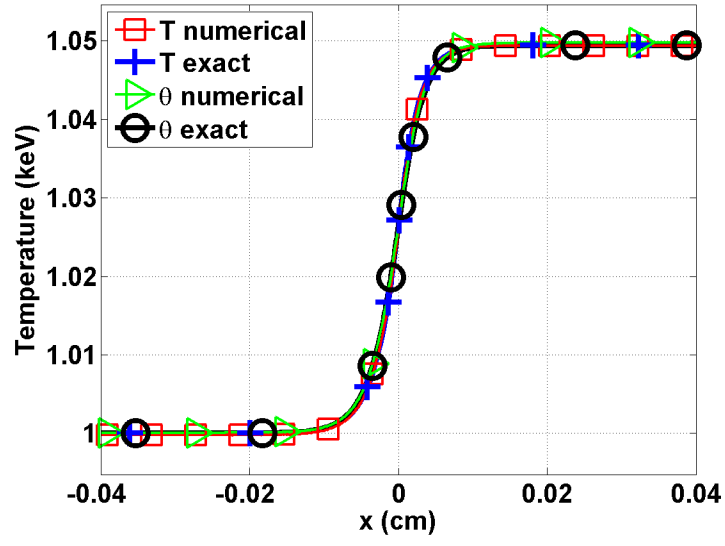
Figure 3.1: Material and radiation temperature profiles at steady state for Mach 1.05 test.
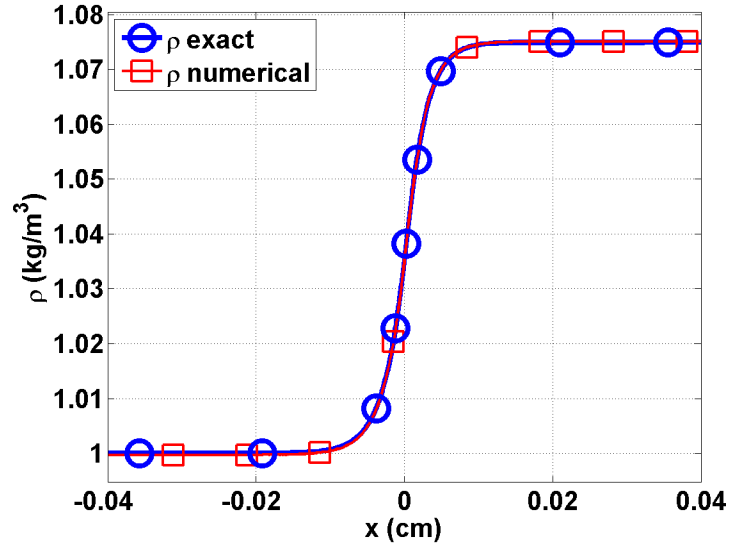
Figure 3.2: Material density profile at steady state for Mach 1.05 test.
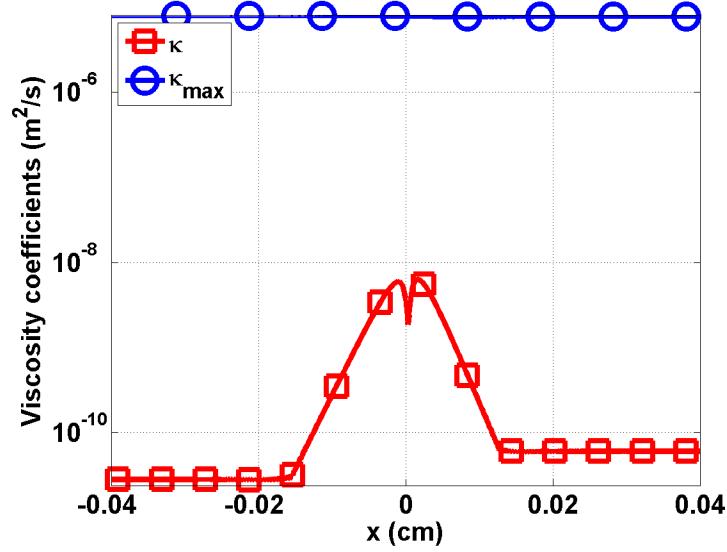
Figure 3.3: First-order viscosity κ_{max} and second-order viscosity κ profiles at steady state for Mach 1.05 test (logarithm scale).

The energy transfer between the material and radiation fields is not large enough to form a shock in the material. Thus, all of the material variables are smooth (Fig. 3.1 and Fig. 3.2) as well as the radiation temperature θ. Because of the smoothness of the solution, the viscosity coefficient κ is three order of magnitude smaller than the first-order viscosity coefficient κ_{max} (Fig. 3.3).

3.4.2.2   A 1.2 Mach hydrodynamic shock

In this test, the material experiences a shock and the radiation energy density remains smooth. The initial conditions, corresponding to a Mach number of 1.2 at the inlet, are as follows:

Table 3.4: Initial conditions for Mach 1.2.

	left	right
$\rho \ (g/cm^3)$	1.	1.0749588
$u \ (cm/sh)$	0.1405588	0.1083456
$T \ (keV)$	0.1	0.1194751
$\epsilon \ (jerks/cm^3)$	$1.372 \ 10^{-6}$	$2.7955320 \ 10^{-6}$

The slab thickness is set to $L = 0.045 \ cm$ and the initial step was located at $x_0 = 0 \ cm$.
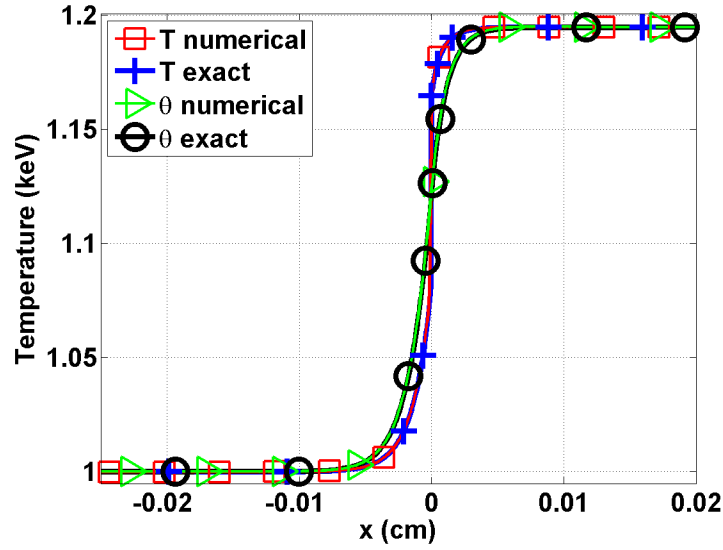
Figure 3.4: Material and radiation temperature profiles at steady state for Mach 1.2 test.

The radiation and material temperatures have two different behaviors (Fig. 3.4):

the later experiences an embedded hydrodynamic shock, whereas the radiation temperature is smooth because of the diffusion term. The material temperature profile does not show any pre- and post-shock oscillations. In Fig. 3.5, the material density profile has a shock as well. The viscosity coefficient (Fig. 3.6) is peaked in the shock as expected but does not saturate to the first-order viscosity. It is conjectured that the diffusion term in the radiation equation brings extra stability to the system. Overall, the numerical solution behaves as expected in the shock and the entropy-based viscosity method seems to efficiently stabilize the numerical scheme.
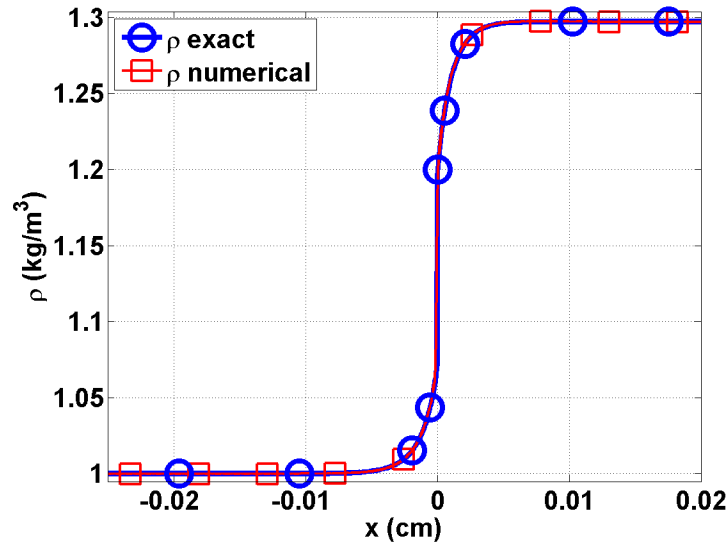
Figure 3.5: Material density profile at steady state for Mach 1.2 test.
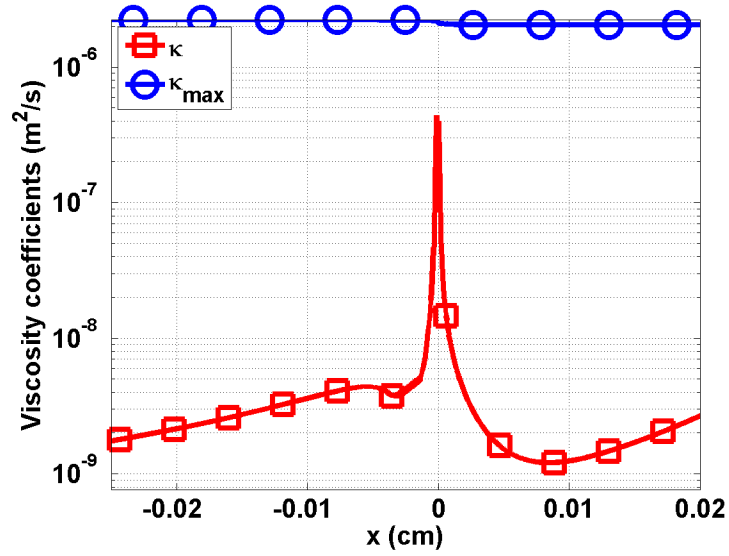
Figure 3.6: First-order viscosity κ_{max} and second-order viscosity κ profiles at steady state for Mach 1.2 test (logarithm scale).

3.4.2.3   A Mach 2 shock

The Mach 2 shock test has two features: a hydrodynamic shock and a Zeldovich spike, which make it interesting for testing the robustness of the entropy-based viscosity method. The initial conditions are specified in Table 3.5 for a slab of length $L = 0.04$ cm with $x_0 = 0.$ cm.

Table 3.5: Initial conditions for Mach 2.

	left	right
ρ (g/cm^3)	1.	1.0749588
u (cm/sh)	0.1405588	0.1083456
T (keV)	0.1	0.1194751
ϵ $(jerks/cm^3)$	1.372 10^{-6}	2.7955320 10^{-6}

Figure 3.7: Material and radiation temperature profiles at steady-state for Mach 2 test.

Once again, the radiation temperature profile is smooth and the material temperature experiences an embedded hydrodynamic shock and a peak as shown in

Fig. 3.7. In Fig. 3.8, the shock is well resolved. The viscosity coefficient profile is given in Fig. 3.9 and is peaked, once again, in the shock region.

For comparison purpose, the same simulation was run with the first-order viscosity only, i.e., κ was set equal to κ_{max} for the whole domain in order to see the advantage of using a second-order viscosity coefficient. The results are given in Fig. 3.10 for the material density and temperature. Numerical solutions with first- and second-order viscosity coefficients are graphed. The radiation temperature profile (not shown here) is not affected much by the first-order viscosity and the curves are coincident. This is expected because of the way the artificial viscosity term is treated in the radiation equation (Section 3.2). However, on the same figure, the shock and peak in the material temperature profile are smoothed out: the shock is not as sharp and the peak amplitude is reduced because of the larger amount of viscosity added to the system. This test shows the benefits of using a high-order viscosity coefficient in order to avoid over-dissipation.
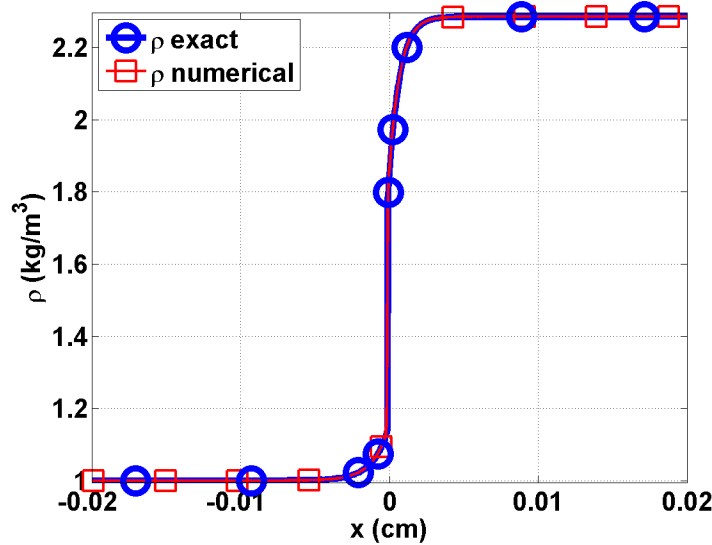

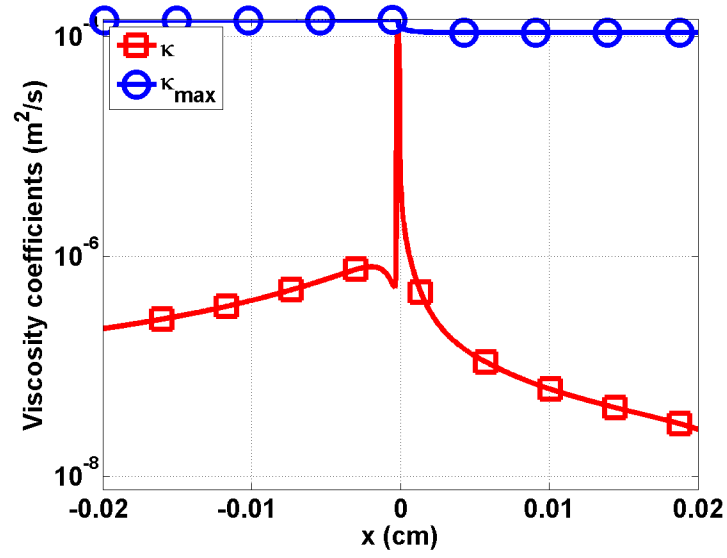Figure 3.8: Material density profile at steady-state for Mach 2 test.

Figure 3.9: First-order viscosity κ_{max} and second-order viscosity κ profiles at steady state for Mach 2 test.
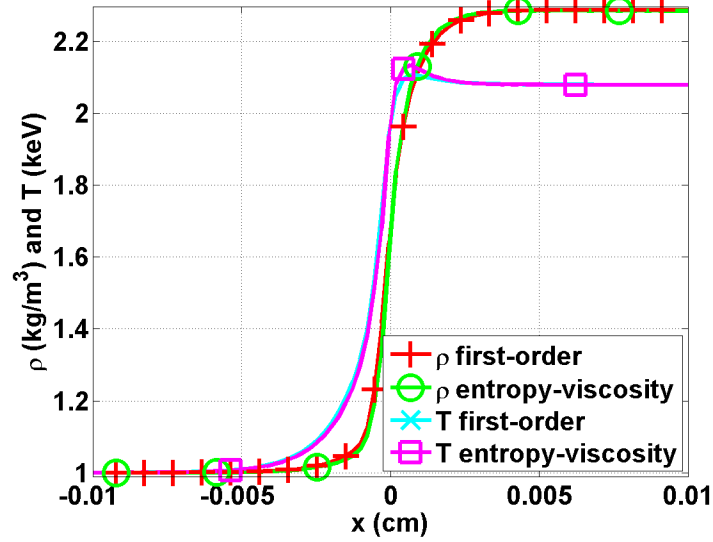

Figure 3.10: Comprarison between the material density and temperature profiles run with the high-order and first-order viscosity coefficients.

A Mach 5 test is run with the initial conditions of Table 3.6 on a computational domain of length $L = 0.05$ *cm* ($x_0 = 0$ *cm*). Steady-state results are shown in Fig. 3.11, Fig. 3.13, and Fig. 3.14 for the material and radiation temperatures, the density and the viscosity coefficients, respectively.

Table 3.6: Initial conditions for Mach 5.

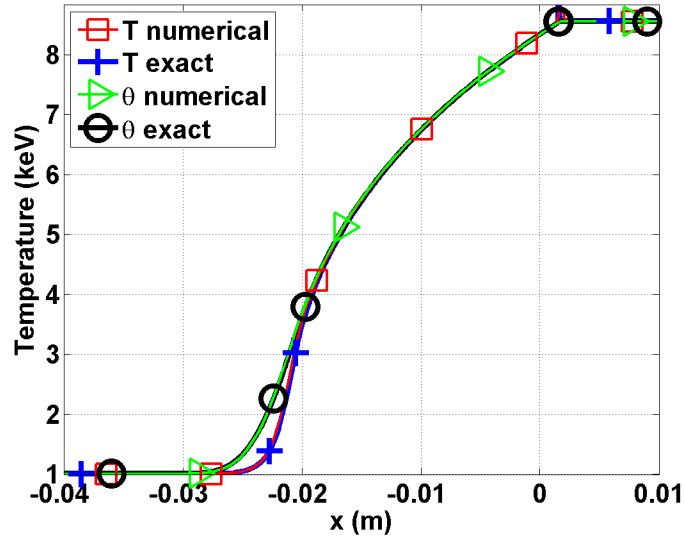|	left	right
ρ (g/cm^3)	1.	1.0749588
u (cm/sh)	0.1405588	0.1083456
T (keV)	0.1	0.1194751
ϵ $(jerks/cm^3)$	$1.372 \ 10^{-6}$	$2.7955320 \ 10^{-6}$

Figure 3.11: Material and radiation temperature profiles at steady state for Mach 5 test. Zoom at the location go the peak using different mesh resolutions.
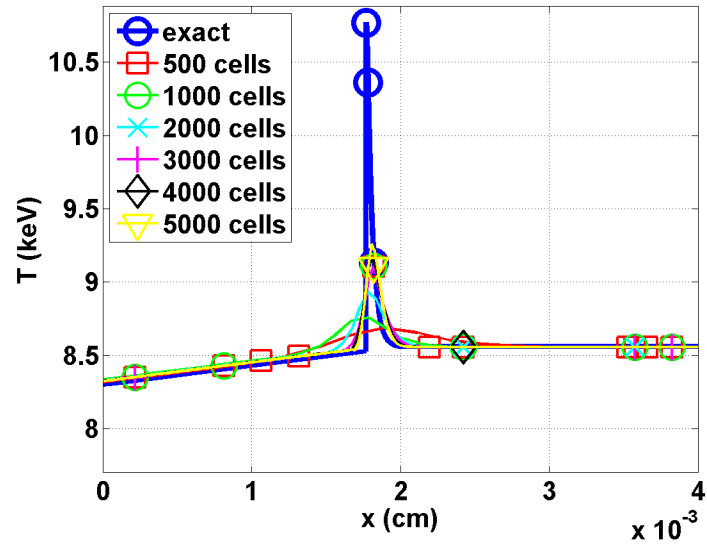

Figure 3.12: Material temperature profiles at steady state for the Mach 5 test in the neighborhood spike.

In Fig. 3.11, the radiation temperature profile is smooth. The material temperature no longer exhibits an embedded hydrodynamic shock but shows a Zeldovich spike. The mesh with 500 elements is not fine enough to correctly resolve the Zeldovich spike. In Fig. 3.12, the Zeldovich spike region is plotted for different mesh resolutions, using from 500 to 5000 elements: the peak is better resolved when using large numbers of elements and its position seems to be independent of the mesh size when appropriately refined. The density profile, Fig. 3.13, shows a shock located at the same position as the Zeldovich spike of the material temperature profile. The viscosity coefficient κ is also peaked in the shock region, as expected. The material and radiation variables do not present any numerical oscillations.
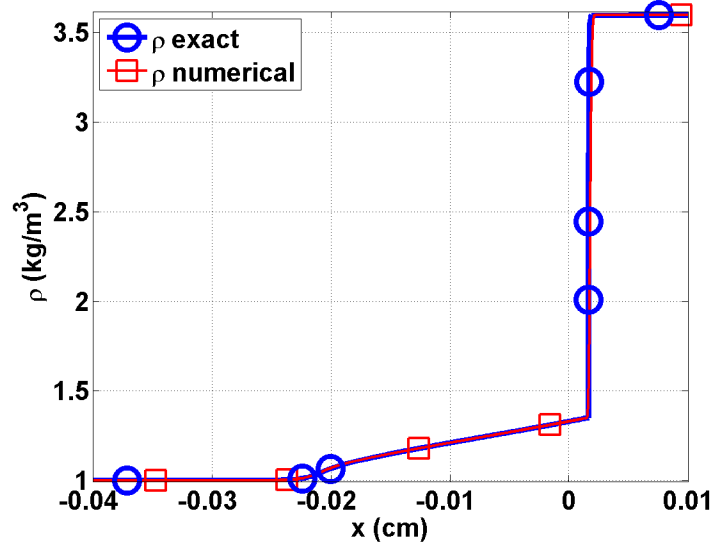

Figure 3.13: Material density profile at steady state for Mach 5 test.
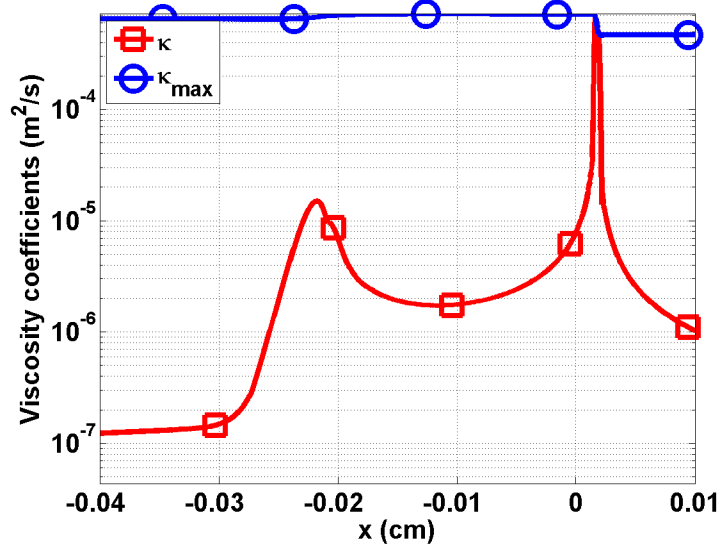
Figure 3.14: First-order viscosity κ_{max} and second-order viscosity κ profiles at steady state for Mach 5 test.

3.4.2.5 Mach 50 shock

The Mach 50 test is known to be challenging. The initial conditions are given in Table 3.7. The computational domain is of length $L = 0.2\ cm$. Results are once again given at steady state.

Table 3.7: Initial conditions for Mach 50.

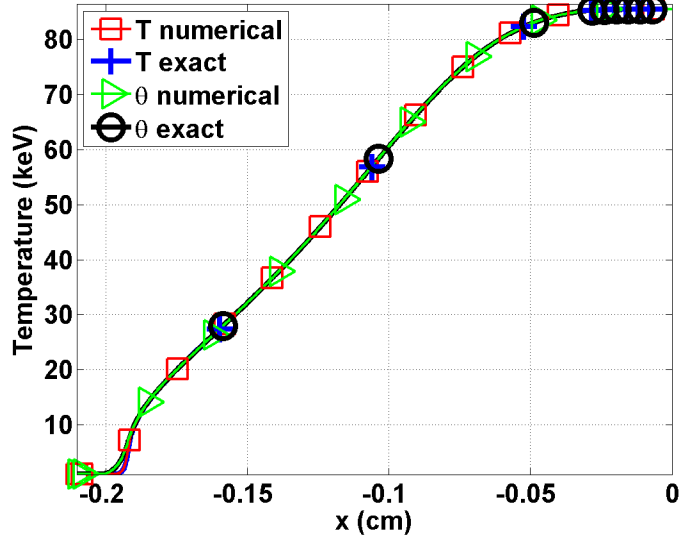|	left	right
$\rho\ (g/cm^3)$	1.	6.5189217
$u\ (cm/sh)$	585.6620	89.84031
$T\ (keV)$	1.0	85.51552
$\epsilon\ (jerks/cm^3)$	$1.372\ 10^{-2}$	$7.33726\ 10^5$

Figure 3.15: Material and radiation temperature profiles at steady state for Mach 50 test.

At Mach 50, there is no embedded hydrodynamic shock forming as shown in Fig. 3.15. The density profile is smooth as shown in Fig. 3.16. In Fig. 3.15, the material and radiation temperatures overlap on all of the computational domain except for a small region located between $x = -0.2$ and $x = -0.18$ cm. In this particular region, the viscosity coefficient saturates to the first-order viscosity (see Fig. 3.17) because of the inflection point in the material temperature profile. The artificial dissipative terms correctly stabilize the material temperature profile without altering the physical solution: the radiation temperature is expected to increase ahead of the material temperature.
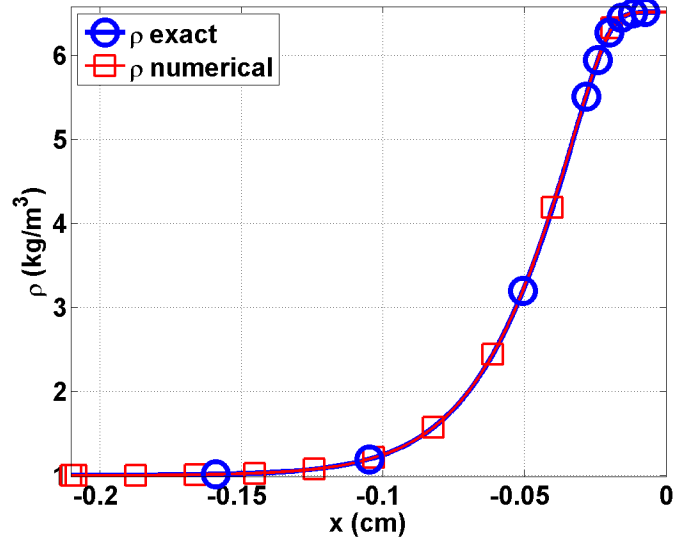
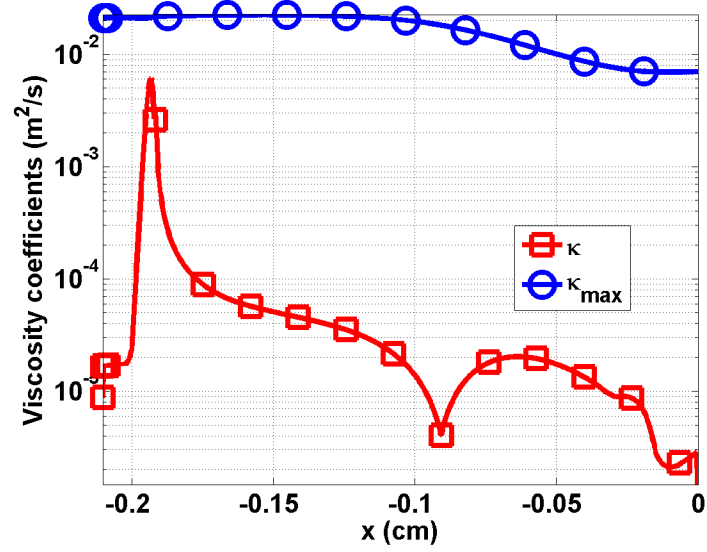Figure 3.16: Material density profile at steady-state for Mach 50 test.

Figure 3.17: First-order viscosity κ_{max} and second-order viscosity κ profiles at steady-state for Mach 50 test.

3.5   Conclusions

In this paper, we have shown that the entropy-based viscosity method is a valid candidate for solving the 1-D radiation-hydrodynamic equations. A theoretical derivation is given for the derivation of the dissipative terms that are consistent with the entropy minimum principle. The viscosity coefficient κ is defined proportional to the entropy residual that measures the local entropy production allowing detection of shocks. Through the manufactured solution method, it is demonstrated, firstly, that second-order accuracy is achieved when the solution is smooth, and secondly, that the artificial dissipative terms do not affect the physical solution in the equilibrium-diffusion limit.

The entropy-based numerical scheme also behaves well in the tests performed for Mach numbers ranging from 1.05 to 50. The main features such as the embedded hydrodynamic shock and the Zeldovich spike are resolved accurately without spurious oscillations. The viscosity coefficient is peaked in the shock region only and behaves as expected. All of these results were obtained by using an unique definition of the viscosity coefficient that is computed on the fly. The addition of dissipative terms to the set of equations requires more computational work but is rather simple to implement.

As future work, extension to the multi-D equations could be considered: all of the derivations presented in this paper hold. The definition of the viscosity coefficients κ and κ_{max} do not need to be modified. It would be interesting to model the radiation equation with an S_n transport approximation and apply the entropy based artificial viscosity to the resultant radiation-hydrodynamics equations. Given the advective nature of the S_n equations, dissipation would need to be added to these equations.

fix spacing in bibliography, if any...

REFERENCES

[1] Perthane B. and Shu C-W. On positivity preserving finite volume schemes for euler equations. *Numer. Math.*, 73:119–130, 1996.

[2] Dinshaw S. Balsara. An analysis of the hyperbolic nature of the equations of radiation hydrodynamics. *J. Quant. Spectrosc. Radiat. Transfer*, 61:617–627, 1999.

[3] G. Hansen D. Gaston, C. Newsman and D. Lebrun-Grandie. A parallel computational framework for coupled systems of nonlinear equations. *Nucl. Eng. Design*, 239:1768–1778, 2009.

[4] Woodward P. R. Dai W. Numerical simulations for radiation hydrodynamics. i. diffusion limit. *Journal of Comput Phys*, 142:182–207, 1998.

[5] J-L. Guermond and B. Popov. Viscous regularization of the euler equations and entropy principles. *under review*, 2012.

[6] Van Rosendale J Hussaini MY, van Leer B. Upwind and high-resolution schemes. *Berlin: Springer*, 12(1):1, 1997.

[7] Leveque R. J. *Numerical methods for conservation laws.* Basel: Birhauser, Reading, Massachusetts, 1990.

[8] B. Popov J-L. Guermond, R. Pasquetti. Entropy viscosity method for nonlinear conservation laws. *Journal Comput. Phys.*, 230:4248–4267, 2011.

[9] R. Pasquetti J-L. Guermond. Entropy viscosity method for high-order approximations of conservation laws. *Lecture Notes in Computational Science and Engineering*, 76:411–418, 2011.

[10] Robert B. Lowrie Jarrod D. Edwards, Jim E. Morel. Second-order discretization in space and time for radiation hydrodynamics. In *International Conference on Mathematics and Computational Methods Applied to Nuclear Science & Engineering (M&C 2013)*, Sun Valley, Idaho, USA, 2013.

[11] Shi Jin and C. David Levermore. Numerical schemes for hyperbolic conservation laws with stiff relaxation terms. *Journal of Computational Physics*, 126:449–467, 1996.

[12] Keyes D. E. Knoll D. A. Jacobian-free newton-krylov methods: a survey of approaches and applications. *Journal of Computational Physics*, 193:357–397, 2004.

[13] P. Lax. Weak solutions of nonlinear hyperbolic equations and their numerical computation. *Comm. Pure Appl. Math.*, 7:159–193, 1954.

[14] Hittinger J. Lowrie R., Morel J. Coupling radiation and hydrodynamics. *Journal Quant. Spectrosc. Radiat. Transfer*, 61:432–500, 1999.

[15] J. D. Edwards R. B. Lowrie. Radiative shock solutions with grey non equilibrium diffusion. *Journal of Comput Phys*, 18:129–143, 2008.

[16] O. LeMetayer R. Berry, R. Saurel. The discrete equation method (dem) for fully compressible, two-phase flows in ducts of spatially varying cross-section. *Nuclear Engineering and Design*, 240:3797–3818, 2010.

[17] J.E. Morel R.B. Lowrie. Issues with high-resolution godunov methods for radiation hydrodynamics. *Journal of Quantitative Spectroscopy & Radiative Transfer*, 69:475–489, 2001.

[18] E. Tadmor. A minimum entropy principle in the gas dynamics equations. *Appl. Numer. Math.*, 2:211–219, 1986.

[19] E.F. Toro. *Riemann Solvers and numerical methods for fluid dynamics.* 2nd Edition, Springer, 1999.

[20] J. Morel V. Zingan, J-L. Guermond and B. Popov. Implementation of the entropy viscosity method with the discontinuous galerkin method. *Journal of Comput Phys*, 253:479–490, 2013.